Victor Henrique Pereira da Rosa

AVALIAÇÃO DE MÉTODOS BASEADOS EM SOLUÇÕES NUMÉRICAS DAS EQUAÇÕES DE REYNOLDS PARA A PREVISÃO DO RUÍDO DE JATOS TURBULENTOS SUBSÔNICOS

Florianópolis

2013

Victor Henrique Pereira da Rosa

AVALIAÇÃO DE MÉTODOS BASEADOS EM SOLUÇÕES NUMÉRICAS DAS EQUAÇÕES DE REYNOLDS PARA A PREVISÃO DO RUÍDO DE JATOS TURBULENTOS SUBSÔNICOS

Dissertação de Mestrado submetido ao Curso de Pós-Graduação em Engenharia Mecânica para a obtenção do Grau de Mestre em Engenharia Mecânica.
Orientador: Prof. César José Deschamps, Ph.D.
Coorientador: Prof. Juan Pablo de Lima Costa Salazar, Ph.D.

Florianópolis

2013

Ficha de identificação da obra elaborada pelo autor,
através do Programa de Geração Automática da Biblioteca Universitária da UFSC.

Rosa, Victor Henrique Pereira da
Avaliação de métodos baseados em soluções numéricas das equações de Reynolds para a previsão do ruído de jatos turbulentos subsônicos / Victor Henrique Pereira da Rosa ; orientador, César José Deschamps ; co-orientador, Juan Pablo de Lima Costa Salazar. - Florianópolis, SC, 2013.
105 p.

Dissertação (mestrado) - Universidade Federal de Santa Catarina, Centro Tecnológico. Programa de Pós-Graduação em Engenharia Mecânica.

Inclui referências

1. Engenharia Mecânica. 2. Aeroacústica. 3. Métodos numéricos. 4. Ruído de jatos. I. Deschamps, César José. II. Salazar, Juan Pablo de Lima Costa. III. Universidade Federal de Santa Catarina. Programa de Pós-Graduação em Engenharia Mecânica. IV. Título.

VICTOR HENRIQUE PEREIRA DA ROSA

AVALIAÇÃO DE MÉTODOS BASEADOS EM SOLUÇÕES NUMÉRICAS DAS EQUAÇÕES DE REYNOLDS PARA A PREVISÃO DO RUÍDO DE JATOS TURBULENTOS SUBSÔNICOS

Esta Dissertação foi julgada adequada para obtenção do Título de Mestre em Engenharia Mecânica e aprovada em sua forma final pelo Programa de Pós-Graduação em Engenharia Mecânica da Universidade Federal de Santa Catarina.

Prof. César José Deschamps, Ph.D. – Orientador

Prof. Juan Pablo de Lima Costa Salazar, Ph.D. – Coorientador

Prof. Armando Albertazzi Gonçalves Jr., Dr.Eng. –
Coordenador do curso

BANCA EXAMINADORA

Prof. César José Deschamps, Ph.D. – Presidente

Prof. Ricardo Eduardo Musafir, D.Sc. (UFRJ)

Prof. Andrey Ricardo da Silva, Ph.D. (UFSC/Joinville)

Prof. Júlio Apolinário Cordioli, Dr.Eng. (UFSC)

À minha esposa,
e eterna namorada,
Nadielli.

AGRADECIMENTOS

Agradeço à CAPES, ao CNPq, à Finep e à Embraer S.A. pelo suporte financeiro.

Ao Marco Aurélio Dellabruna Maccarini e à Lígia Venancio Froening por me apresentarem seu trabalho experimental, possibilitando-me maior entendimento sobre jatos turbulentos.

Ao Marco Carrilho Diniz pela revisão deste manuscrito, apresentando o ponto de vista muito proveitoso de um pesquisador não familiarizado com aeroacústica.

Ao Rafael Costa Engel pelas discussões sobre aeroacústica e pela disponibilização de dados de suas simulações numéricas. Estendo o agradecimento ao Filipe Dutra da Silva por ter participado no desenvolvimento dessas simulações, pelas discussões sobre o tema e pela revisão deste manuscrito.

Aos professores membros da banca por aceitarem o convite, pelos indispensáveis comentários ao manuscrito e pelas discussões durante a defesa.

Ao Carlos Roberto Ilário da Silva pela disponibilização de dados de suas simulações numéricas, pela coautoria em artigos científicos e pela ajuda indispensável no direcionamento desta dissertação.

Aos meus orientadores pelo direcionamento deste trabalho, pela motivação, pela revisão do manuscrito e por depositarem confiança em mim, dando-me a oportunidade de realizar este trabalho.

In all science, error precedes the truth, and it is better it should go first than last.

Hugh Walpole

RESUMO

Nesta dissertação são avaliados métodos que utilizam a solução numérica das equações de Reynolds para a previsão do ruído de jatos. As condições de escoamento são caracterizadas por número de Reynolds em torno de 10^6, números de Mach entre 0.50 e 1.00, jatos isotérmicos e aquecidos, originados por bocais circulares simples e coaxiais com e sem serrilhas. A previsão do ruído de jatos pode ser dividida em duas etapas: o cálculo da intensidade das fontes sonoras e a avaliação dos efeitos de refração sonora. Quatro métodos para cálculo da intensidade das fontes sonoras encontrados na literatura são implementados para fins de comparação, dois baseados na Equação de Lighthill e dois a partir das Equações Linearizadas de Euler. De forma geral, os resultados dos métodos baseados nas duas formulações apresentam boa concordância com dados experimentais, mas os métodos baseados na Equação de Lighthill possuem uma formulação mais simples e necessitam de um menor número de constantes empíricas. A técnica de traçado de raios é utilizada para avaliar a refração das ondas de pressão acústica emitidas por fontes do tipo monopolo localizadas em diferentes posições do jato. Três aspectos relacionados à refração são estudados em detalhes: (i) a dependência da zona de silêncio com a posição da fonte, (ii) a importância de gradientes de velocidade do som em jatos aquecidos, e (iii) a assimetria originada por bocais serrilhados. Devido à acurácia e ao baixo custo computacional, conclui-se que os métodos estudados são alternativas viáveis para a análise do ruído de jatos.

Palavras-chave: Ruído de jatos, Analogia Acústica de Lighthill, Equações Linearizadas de Euler, efeitos da refração, técnica de traçado de raios.

ABSTRACT

In this dissertation methods based on the numerical solution of the Reynolds-averaged Navier–Stokes equations are evaluated to predict jet noise. The flow conditions include Reynolds number around 10^6 and Mach number in the 0.50–1.00 range, isothermal or heated fluid streams, single- and dual-stream circular nozzles with or without chevrons. The prediction of jet noise can be split in two components: the evaluation of the strength of sound sources and the evaluation of the effects of sound refraction. Four methods available in the literature are implemented to evaluate the source strength; two based on the Lighthill Equation and two based on the Linearized Euler Equations. It is found that both frameworks allow predictions of noise spectra in reasonable agreement with experimental data. However, the methods based on the Lighthill Equation offer a more straightforward formulation and need less empirical constants. A ray tracing method is also adopted to study the effects of refraction on acoustic pressure waves emitted from monopole sources in several positions within the jet. Three aspects of refraction are studied in detail: (i) the dependence of the zone of silence regarding the source position, (ii) the significance of sound speed gradients in heated jets, and (iii) the asymmetry created by chevron nozzles. Given the reasonable accuracy and low computational cost of the studied methods, the so-called RANS-based methods are considered a viable approach to predict jet noise.

Keywords: Jet noise, Lighthill Acoustic Analogy, Linearized Euler Equations, refraction effects, ray tracing technique.

LIST OF FIGURES

LIST OF TABLES

LIST OF ABBREVIATIONS AND ACRONYMS

BPR	Bypass Ratio
DNS	Direct Numerical Simulation
EPNdB	Effective Perceived Noise in deciBels
FAA	Federal Aviation Administration
ICAO	International Civil Aviation Organization
LEE	Linearized Euler Equations
LES	Large Eddy Simulation
LRT	Lighthill Ray Tracing
PNL	Perceived Noise Level
PSD	Power Spectral Density
RANS	Reynolds-Averaged Navier-Stokes
RSM	Reynolds-Stress Transport Model
SPL	Sound Pressure Level
TET	Turbulent Energy Transfer
TR	Temperature Ratio

NOMENCLATURE

Roman

A	Ray tube area
a	Speed of sound
c_A	Empirical constant related to an overall amplitude
c_τ	Empirical constant related to the turbulent time scale
c_ℓ	Empirical constant related to the turbulent length scale
C	Constant factor
$C_{k^{7/2}}$	Coefficient related to the distribution of $k^{7/2}$ in the jet
$C^{\mathrm{dB}}_{k^{7/2}}$	$C_{k^{7/2}}$ in decibels
D	Nozzle diameter
$\mathbf{e}$	Viscous stress tensor
$\mathbf{F}$	Source term in momentum equations
f	Linear frequency
f_s	Source characteristic frequency
k	Mean turbulent kinetic energy per unit mass
ℓ_s	Source characteristic length scale
M	Mach number
N	Number of rays crossing a far field area
P_{ref}	Reference pressure, defined at the threshold of hearing
p	Fluid pressure
p_a	Adjoint pressure
p_{turb}	Turbulent pressure
Re	Reynolds number
$R_{\phi\phi}$	Autocorrelation of ϕ
r	Distance between the observer and the nozzle exit
S	Power spectral density of the acoustic pressure
$\mathbf{s}$	Wave-slowness vector
$\mathbf{T}$	Lighthill stress tensor
t	Time coordinate
TR	Temperature Ratio

$\mathbf{U}$	Velocity vector
$\mathbf{u}$	Turbulent velocity fluctuations
u_s	Source characteristic turbulent velocity
$\mathbf{V}_{\text{ray}}$	Ray velocity
V	Volume of an interval of integration
$\mathbf{v}$	Fluid molecule velocity
VR	Velocity Ratio
$\mathbf{x}$	Cartesian coordinate
$\mathbf{x}_{\text{ray}}$	Ray position
$\mathbf{y}$	Observer position

Greek

δ_{ij}	Kronecker delta
$\delta(\phi)$	Dirac delta function evaluated at ϕ
ε	Mean turbulent dissipation rate per unit mass
γ	Ratio of specific heats
ν	Kinematic viscosity
Ω	Instante in time defining a wavefront
φ	Azimuthal angle
Π	Logarithmic pressure
Π_g	Green function corresponding to Π
ρ	Fluid density
τ	Separation in time
θ	Polar angle
Θ	Source term in continuity equation
$\boldsymbol{\xi}$	Space separation vector

Subscripts

jet	Property at the nozzle exit
i	(i)th component of a vector
i, j	(i, j)th component of a tensor
∞	Reference property evaluated at the observer position
p	Related to primary stream

s	Related to secondary stream

Symbols

$\langle\phi\rangle$	Mean value of ϕ
ϕ'	Acoustic fluctuations of ϕ

CONTENTS

1 INTRODUCTION

This dissertation was developed in the context of the Brazilian research project *Aeronave Silenciosa* (Silent Aircraft), which is a joint effort between academia and industry to study external aircraft noise. The emphasis is on jet noise generated by the interaction between the ambient air and high-speed gas leaving the aircraft engine. The objective is the assessment of fast numerical methods available in the literature to predict jet noise, considering accuracy and computational cost.

1.1 AIRCRAFT NOISE

During all phases of flight, the aircraft engine generates noise that propagates into the cabin and to the external ambient. Whereas the noise inside the aircraft is heard only by the passengers and crew, the external noise affetcs a larger group of people during approach and take-off. Noise exposure is a significant cause of discomfort for people in airport surroundings and can lead to several chronic diseases. It is known that exposure to moderate to high levels of noise can cause hearing impairment, and recent studies show that noise is also related to hypertension, psychological dysfunctions, poor performance of children at school, among other negative effects (MORREL; TAYLOR; LYLE, 1997; HAINES et al., 2001; FRANSSE et al., 2004; GREISER; GREISER; JANHSEN, 2007; ERIKSSON et al., 2007; JARUP et al., 2008). In addition to health problems, the discomfort created by noise has a significant impact on public opinion. The International Civil Aviation Organization (ICAO) considers noise the main cause of community aversion to airport operations (ICAO, 2010). This aversion is translated into public policies that hinder the installation of new airports or limit the opening hours of existing airports. Considering the negative impact of aircraft noise and the increasing importance of aviation for transportation, noise is an important element in the aircraft design process.

The first civil aircraft powered by turbojet engines (Figure 1.2) entered operation in the 1950s (SMITH, 1989) and began to replace the propellers used since the earliest aircraft. The turbojets were in many aspects superior to the propeller engines, although much noisier. As the number of turbojet-powered aircraft rose rapidly during the late 1950s, the high level of noise emitted by these aircraft created a negative effect

on the public as a whole. Political concern with aircraft noise increased considerably in the 1960s, inducing the International Civil Aviation Organization (ICAO) and the Federal Aviation Administration (FAA) to issue the first international regulations on aircraft noise in the early 1970s (SMITH, 1989). Figure 1.1 shows the regulation levels (*chapters 2*, *3*, and *4*) in *Effective Perceived Noise in decibels* (EPNdB)—the standard unit in certification procedures, which considers the measured sound pressure level and corrections related to the frequency spectrum and exposure duration. In addition to the international regulations presented in Figure 1.1, many airports impose stricter rules. Therefore, the industry is required to design quieter aircraft to comply with the international regulation and also to gain market share.

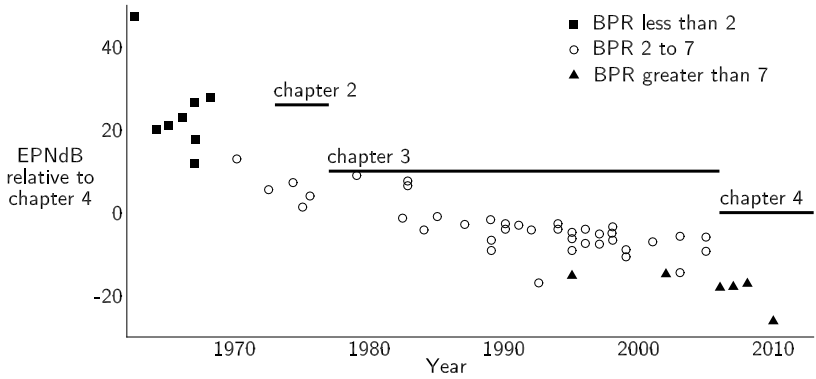

Figure 1.1 – Noise level regulations and examples of certified aircraft grouped by bypass ratio (BPR), defined as the ratio of secondary- and core-stream mass flow rates. Adapted from (ICAO, 2010).

The turbofan engine, shown in Figure 1.2, was introduced in the 1970s, representing a breakthrough in aircraft technology since the advent of the turbojets. Conversely to the single-stream jet issued from turbojets, the turbofan engine generates a dual-stream jet and can be designed to produce different bypass ratios. Figure 1.3 shows that a higher bypass ratio (high-BPR) is related to lower noise levels.

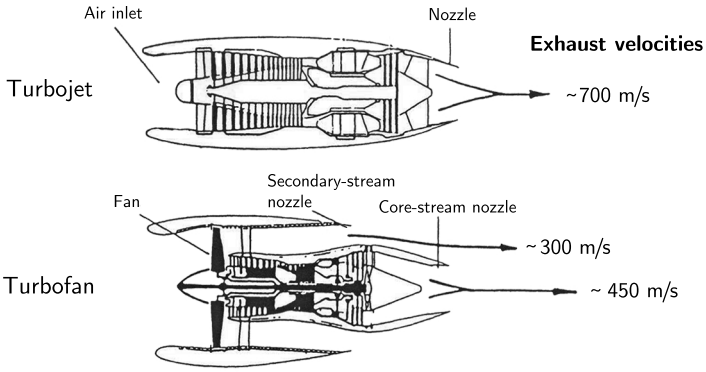

Figure 1.2 – Typical turbojet and turbofan engines. Adapted from (SMITH, 1989).

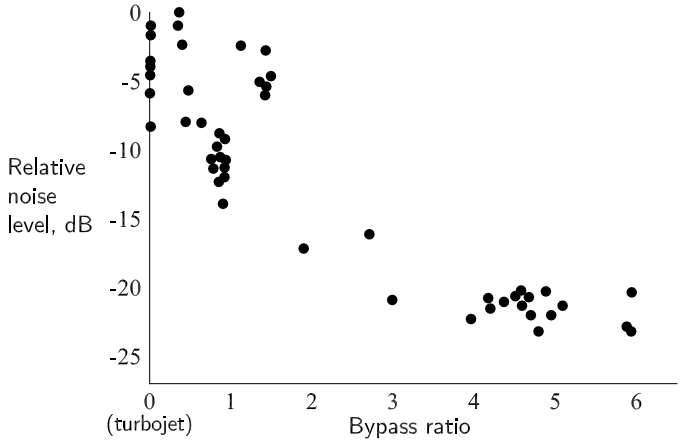

Figure 1.3 – Relation between noise level and bypass ratio. Adapted from (SMITH, 1989).

The high-BPR turbofan decreased jet noise to such low levels that previously unimportant sources of noise started to have influence in the overall aircraft noise (SMITH, 1989). The sources of external aircraft noise can be divided into two groups: airframe and engine noise. Airframe noise relates to the non-propulsive components of aircraft (fuselage, landing gear, slats, flaps, pylons). On the other hand, engine

noise is generated by the components related to generation of thrust. Whereas most of such components (fan, turbines, combustion core) generate noise inside the engine nacelle, jet noise is generated outside the engine by the interaction of the exhaust gases and the external flow. Table 1.1 shows a comparison of noise levels emitted by the different sources of a typical turbofan-powered aircraft. The noise levels change with the phase of flight: whereas at approach airframe and engine noise are significant, at take-off the bulk of noise is generated by the engine. Jet noise also depends on the phase of flight: it is much louder at take-off, while the engine is at full power in order to provide the necessary thrust to accelerate the aircraft. Although jet noise importance was reduced with the advent of the turbofan, Table 1.1 shows that it is still a significant source of aircraft noise, which justifies its study in the *Aeronave Silenciosa* project.

Table 1.1 – Maximum PNL[a] of a typical turbofan-powered aircraft. Adapted from (NASA, 1999).

	Component	Approach	Take-off
	Airframe	102.1 dB	79.7 dB
engine	Fan	106.3 dB	100.7 dB
engine	Jet	86.0 dB	99.1 dB
	Total[b]	108.0 dB	103.1 dB

[a] *Perceived noise level*, a certification unit similar to EPNdB.
[b] Including other noise components not shown in the table.

1.2 JET AEROACOUSTICS

While studying noise generated by turbulent jets, Sir Michael James Lighthill wrote two papers (LIGHTHILL, 1952, 1954) that established the foundations of aeroacoustics. More than two decades later, Goldstein (1976) wrote the first book entirely dedicated to aeroacoustics, in which he stated:

> Aeroacoustics is concerned with sound generated by aerodynamic forces or motions originating in a flow rather than by the externally applied forces or motions of classical acoustics. Thus, the sounds generated by vibrating violin strings and loudspeakers fall into the category of classical acous-

tics, whereas sounds generated by the unsteady aerodynamic forces on propellers or by turbulent flows fall into the domain of aeroacoustics. The term "aerodynamic sound" introduced by Lighthill (who developed the foundations of this field) is also frequently used.

Smith (1989) follows with a book about aircraft noise, in which he highlights the significance of jet noise for the aeronautical industry. An important element of aeroacoustics research is the understanding of turbulent jets, which is covered in several books on fluid dynamics (HINZE, 1975; TRITTON, 1988; POPE, 2000; MATHIEU; SCOTT, 2000). In this section aspects of turbulent jets and the associated acoustic noise are discussed.

Tritton (1988) states that "a jet is produced when fluid is ejected from an orifice". Figure 1.4 shows a low-Reynolds-number jet, with the Reynolds number defined by

$$\mathrm{Re} = \frac{\mathrm{U_{jet}} \mathrm{D_{jet}}}{\nu} \tag{1.1}$$

where $\mathrm{U_{jet}}$ is the jet characteristic velocity, $\mathrm{D_{jet}}$ the nozzle diameter and ν the average kinematic viscosity at the nozzle exit. Figure 1.4 (a) shows how the laminar flow inside the duct becomes turbulent downstream of the nozzle exit. This is the result of instabilities in the shear layer created between the jet and the external flow.

The jet flow considered in this study is at high Reynolds number ($\sim 10^6$) and, therefore, it is already turbulent at the nozzle exit. In such a case, turbulence is generated in the shear layer and turbulence intensity is increased downstream of the nozzle exit. Figure 1.4 (b) shows a long-exposure photograph that represents the characteristics of the mean flow and, hence, it is not possible to distinguish transient effects such as the large turbulent-scales so clearly visible in Figure 1.4 (a). Nevertheless, the mean flow can give useful information about turbulence for acoustic prediction methods that are presented in Chapters 2 and 3.

Figure 1.5 shows the profiles of mean axial velocity, $\langle U_1 \rangle$, and the root-mean-square of the axial velocity fluctuation, $\left\langle u_1^2 \right\rangle^{1/2}$, where $u_1 \equiv U_1 - \langle U_1 \rangle$, and U_1 is the instantaneous velocity in the downstream direction. Figure 1.6 presents information about the mean turbulent kinetic energy per unit mass,

$$k \equiv \frac{1}{2} \left\langle u_i u_i \right\rangle , \tag{1.2}$$

indicating that the turbulence is maximum on the shear layer centerline.

Following the theory that will be presented in Chapter 2, the intensity of jet mixing noise, which is related to the fine-scale turbulence, is proportional to $k^{7/2}$; so we identify in Figure 1.6 the regions where most of jet mixing noise is generated. Although other types of noise sources exist in jets (TAM et al., 2008), the methods presented in Chapter 2 only consider jet mixing noise.

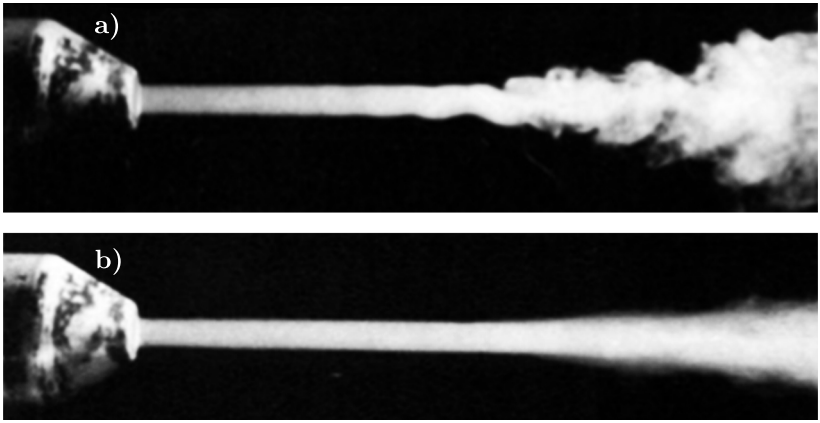

Figure 1.4 – Jet flow with Reynolds number of 1690. Photographs with relatively (a) short and (b) long exposures. Air stream is made visible with oil smoke. Adapted from (BECKER; MASSARO, 1968).

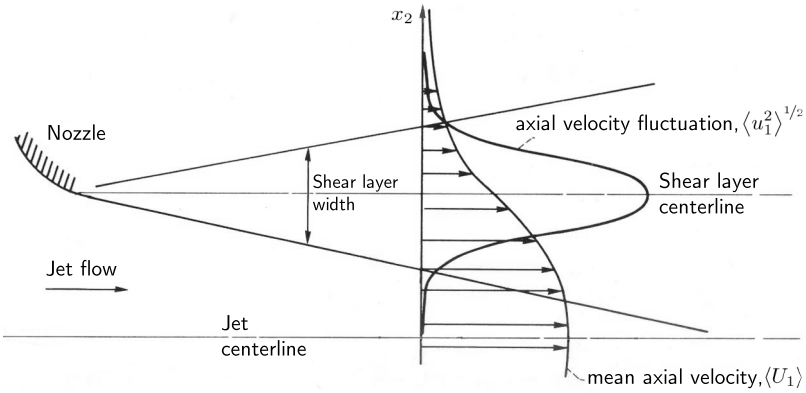

Figure 1.5 – Profiles of mean axial velocity and root-mean-square of the axial velocity fluctuation. Adapted from (GOLDSTEIN, 1976).

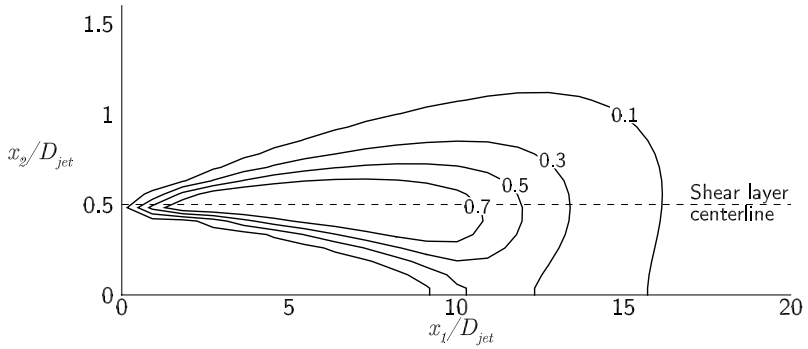

Figure 1.6 – Lines of constant $\left(\frac{k}{k_{\max}}\right)^{7/2}$, where $k_{\max}$ is the maximum mean turbulent kinetic energy per unit mass in the jet, for a cold single-stream jet with $M_{jet} = 0.75$ (numerical simulation from (ILáRIO, 2011)). The vector x_i defines the cartesian coordinate system, with x_1 being aligned with the jet axis.

Since jet noise is generated in a large region outside the engine nacelle (for more than ten diameters downstream the nozzle exit), it is not possible to act directly at the source location to reduce jet noise. In fact, it is necessary to modify the flow before it leaves the nozzle in such a way that the resulting jet will generate less noise. This was initially achieved with the replacement of turbojets by turbofans by using a secondary stream with a greater area so that the same thrust can be generated with a lower exit velocity (Figure 1.2). By having two jet streams the interaction between the jet and the external flow generates less turbulence and noise than in the case of turbojets. Improvements of the early turbofans were achieved by increasing the BPR by more than seven (Figure 1.1). Unfortunately, further increases of the BPR are limited by other aspects of aircraft design, so novel approaches to reduce jet noise are necessary.

Significant research has been focused on the assessment of non-axisymmetric nozzle geometries in the past two decades. Two promising ideas are chevrons nozzles (CALLENDER; GUTMARK; MARTENS, 2003; BRIDGES; BROWN, 2004) and non-coaxial dual-stream nozzles (MEAD; COPPLESTONE, 1998). These nozzles have a complex effect on the emitted noise that, unlike the noise reduction achieved by increasing the BPR of turbofans, cannot be predicted in a straightforward manner by scaling laws or extrapolated from empirical databases. The first conclusions about these nozzles were drawn from experimental studies,

which are expensive and time-consuming. Thus, faster methods are necessary to further develop these design ideas.

1.3 COMPUTATIONAL AEROACOUSTICS

Computational aeroacoustics (CAA) is associated with the simulation of sound generated by unsteday flow. Most of the recent advances in CAA are concerned with high-resolution transient simulations, such as Direct Numerical Simulation (DNS) and Large Eddy Simulation (LES) (TAM, 1995; COLONIUS; LELE, 2004; TAM, 2006; WANG; FREUND; LELE, 2006; BODONY; LELE, 2008; KARABASOV, 2010; KARABASOV et al., 2010; ASTLEY; GABARD, 2011a, 2011b).

Because of restrictions concerning the geometry and Reynolds number, DNS is applied to study the mechanics of noise generation in more fundamental cases. Wei and Freund (2006) used DNS computations to study noise control in a shear layer and showed that a decrease of 11dB can be achieved without large-scale changes in flow features (such as turbulent kinetic energy field and mean flow spreading rate). On the other hand, LES is being used to more practical cases, such as the prediction of noise emitted by chevron nozzles (XIA; TUCKER; EASTWOOD, 2009). Despite their good accuracy, DNS and LES methods are too computationally expensive to be used as a design tool in the development of quieter nozzles.

Methods based on RANS simulations are faster, alternative approaches. Specifically for the prediction of jet noise, MGBK (KHAVARAN; KREJSA; KIM, 1992; KHAVARAN; KREJSA, 1998) is the earliest so-called RANS-based method. The MGBK method uses the Lighthill Equation (LIGHTHILL, 1952) to model the strength of acoustic sources and the Lilley Equation (LILLEY, 1974) to model the sound-flow interaction. The information about turbulence is obtained from a RANS simulation with a $k - \varepsilon$ turbulence model.

Tam and Auriault (1999) developed a similar method that uses a RANS solution, but has the source strength formulation based on an analogy with the kinetic gas theory and the sound-flow interaction evaluated with the Linearized Euler Equations (LEE). Jet3D (HUNTER, 2002) is another method based on the Lighthill Equation and RANS simulations. Morris and Farassat (2002) compare the source strength formulation proposed by Tam and Auriault (1999) with a method based on the Lighthill Equation. The comparison shows that the formulation proposed by Tam and Auriault (1999) yields better results for an observer at 90° in relation to the jet axis.

Morris and Boluriaan (2004) present a method based on the LEE for the evaluation of the sound-flow interaction and a source term related to turbulent velocity correlations. JeNo (KHAVARAN; BRIDGES, 2004) numerically solves the Lilley and RANS equations to evaluate jet noise. Azarpeyvand (2008) modified the MGBK method so that a new time scale could be defined to relate turbulent properties with the acoustic source. Ilário (2011) presented a method referred to as Lighthill Ray Tracing (LRT) that uses the Lighthill Equation to evaluate the source strength and a ray tracing technique to evaluate sound refraction caused by the flow. LRT also incorporates a new time scale proposed by Azarpeyvand (2008).

The aforementioned methods share in common the use of equations (Lighthill Equation, Lilley Equation or the Linearized Euler Equations) that model sound propagation, which have a source term dependent on correlations of turbulent properties. Moreover, each method models turbulent correlations as a function of empirical constants and information from the mean flow gathered from the numerical solution of RANS equations. As an exception, LRT (ILáRIO, 2011) uses a ray tracing method to evaluate the sound-flow interaction effects.

1.4 OBJECTIVES OF THIS DISSERTATION

This dissertation makes an assessment of the source strength models presented by Tam and Auriault (1999), Morris and Farassat (2002), Morris and Boluriaan (2004), and Ilário (2011). Hereafter, these methods are named after their primary references, the only exception being *LRT (2011)*, presented by Ilário (2011). Note that when referring to the method presented by Tam and Auriault (1999), for example, the text is printed in italics, as in *Tam and Auriault (1999)*, whereas when referreing to the reference, the text is printed in roman type as usual. The most important difference between the methods is the sound propagation equations upon which they are based. The methods *Morris and Farassat (2002)* and *LRT (2011)* are based on the Lighthill Equation, whereas *Tam and Auriault (1999)* and *Morris and Boluriaan (2004)* are based on the Linearized Euler Equations. Another difference is the used semi-empirical models for turbulent correlations. The methods also differ by the way the effects of sound-flow interaction are treated. For simplicity, the evaluation of sound-flow interactions is initially avoided by computing the noise for an observer at 90° to the jet axis, where sound-flow interactions are known to be negligible. However, the ray tracing technique implemented by Ilário (2011) is subsequently used to study sound refraction in subsonic jets.

The main goal is to assess the aforementioned RANS-based methods as a numerical tool for the development of quieter nozzles.

1.5 DISSERTATION OUTLINE

The four source models considered in the study are detailed in Chapter 2, followed by the presentation of the ray tracing technique in Chapter 3. The nozzle geometries, operating conditions, and the results of the investigated cases are given in Chapter 4. Finally, the main conclusions and suggestions for future work are discussed in Chapter 5.

2 SOURCE STRENGTH MODELS

Noise can be distinguished by the magnitude and frequency of pressure fluctuations. The pressure fluctuation p' related to sound waves, or simply acoustic pressure, is defined as

$$p' \equiv p - \langle p \rangle \,, \tag{2.1}$$

where p is the instantaneous fluid pressure, and $\langle p \rangle$ is the mean pressure.

The power spectral density (PSD) is a mathematical quantity that carries information about the magnitude and frequency of p', and is given by

$$\mathrm{S}\left(\mathbf{y}, f\right) = \int_{-\infty}^{\infty} R_{p'p'}\left(\mathbf{y}, \tau\right) e^{-2\pi i f \tau} \mathrm{d}\tau, \tag{2.2}$$

where it is made explicit the dependence of S with the observer position, $\mathbf{y}$, and with the frequency, f; $R_{p'p'}$ is the autocorrelation of the acoustic pressure; and τ is a separation in time (SHIN; HAMMOND, 2008). For a stationary process, the autocorrelation can be estimated by

$$R_{p'p'}\left(\mathbf{y}, \tau\right) = \left\langle p'\left(\mathbf{y}, t\right) p'\left(\mathbf{y}, t+\tau\right) \right\rangle . \tag{2.3}$$

Substitution of Equation (2.3) in Equation (2.2), yields

$$\mathrm{S}\left(\mathbf{y}, f\right) = \int_{-\infty}^{\infty} \left\langle p'\left(\mathbf{y}, t\right) p'\left(\mathbf{y}, t+\tau\right) \right\rangle e^{-2\pi i f \tau} \mathrm{d}\tau, \tag{2.4}$$

which is the equation used by the source strength models presented in this chapter to quantify jet noise.

In order to compare numerical results with experimental data, the PSD is evaluated in decibel [dB] scale as the sound pressure level (SPL) by

$$\mathrm{SPL} = 10 \log_{10} \frac{\mathrm{S}}{P_{\mathrm{ref}}^2}, \tag{2.5}$$

where S is the PSD calculated from each method and $P_{\mathrm{ref}} = 20\mu\mathrm{Pa}$ is the reference pressure.

In the following sections, the Lighthill Acoustic Analogy, the Linearized Euler Equations and the four RANS-based sources strength methods are presented. The objective is to provide enough information to allow both the implementation of the methods and the identification of their most important differences.

2.1 LIGHTHILL ACOUSTIC ANALOGY

Lighthill (1952, 1954) presented a theory to evaluate sound generated by turbulent jets that established the foundations of aeroacoustics.

Using the summation convention, the continuity and momentum equations can be written as

$$\frac{\partial \rho}{\partial t} + \frac{\partial \rho U_j}{\partial x_j} = 0, \tag{2.6}$$

and

$$\rho \left(\frac{\partial U_i}{\partial t} + U_j \frac{\partial U_i}{\partial x_j} \right) = -\frac{\partial p}{\partial x_i} + \frac{\partial e_{ij}}{\partial x_j}, \tag{2.7}$$

where ρ is the fluid density, U_i is the (i)th component of the velocity vector, and e_{ij} is the (i,j)th component of the viscous stress tensor. On multiplying Equation (2.6) by U_i, adding the result to Equation (2.7), and combining the results yields

$$\frac{\partial \rho U_i}{\partial t} = -\frac{\partial}{\partial x_j} \left(\rho U_i U_j + \delta_{ij} p - e_{ij} \right), \tag{2.8}$$

where δ_{ij} is the Kronecker delta. Adding $a_\infty^2 \partial \rho / \partial x_i$ to both sides of Equation (2.8), where a_∞ is a reference sound speed, yields

$$\frac{\partial \rho U_i}{\partial t} + a_\infty^2 \frac{\partial \rho}{\partial x_i} = -\frac{\partial T_{ij}}{\partial x_i}, \tag{2.9}$$

where T_{ij} is the (i,j)th component of the Lighthill stress tensor, given by

$$T_{ij} \equiv \underbrace{\rho U_i U_j}_{\text{intertial term}} + \underbrace{\delta_{ij} \left[(p - p_\infty) - a_\infty^2 (\rho - \rho_\infty) \right]}_{\text{entropic term}} - \underbrace{e_{ij}}_{\text{viscous term}}. \tag{2.10}$$

Taking the divergence of Equation (2.9), differentiating Equation (2.6) with respect to t, and subtracting the results, the Lighthill Equation is obtained

$$\frac{\partial^2 \rho'}{\partial t^2} - a_\infty^2 \frac{\partial^2 \rho'}{\partial x_i \partial x_i} = \frac{\partial^2 T_{ij}}{\partial x_i \partial x_j}, \tag{2.11}$$

which has the form of the wave equation with the source term $\frac{\partial^2 T_{ij}}{\partial x_i \partial x_j}$. Although the source term depends on the solution of the wave equation (ρ' is the solution of the wave equation and is present in the source

term), it is possible to consider it independent because sound carries such a small part of the flow energy that the effects of sound on the flow can be ignored. Assuming that sound radiates from the jet to an infinite homogeneous fluid without the influence of solid boundaries, it follows that Equation (2.11) has a solution in terms of the free-space Green's function:

$$\rho'(\mathbf{y},t) = \frac{1}{4\pi a_\infty^4} \iiint_{V(\mathbf{x})} \frac{(y_i - x_i)(y_j - x_j)}{|\mathbf{y}-\mathbf{x}|^3} \frac{\partial^2}{\partial t^2} T_{ij}\left(\mathbf{x}, t - \frac{|\mathbf{y}-\mathbf{x}|}{a_\infty}\right) \mathrm{d}\mathbf{x}. \tag{2.12}$$

Lighthill (1952) used this solution to develop a scaling law, referred to as Lighthill's eighth power law, that predicts the acoustic power output as a function of jet speed.

Lush (1971) showed that Lighthill's theory fails to predict the sound intensity for certain observer positions. He attributed part of the errors to the fact that Lighthill's Equation ignores sound-flow interactions such as the refraction caused by the mean velocity gradients in the jet shear layer. Therefore, Equation (2.12) is accurate if the observer is positioned at $\theta = 90°$ in relation to the jet axis (see Figure 2.1 for the coordinate system), where sound-flow interaction effects are known to be negligible.

In order to circumvent the aforementioned problem, more complex equations to evaluate sound propagation that take into account effects of sound-flow interaction can be used (Lilley (1974), Tam and Auriault (1999), for example). Ilário (2011), on the other hand, uses the Lighthill Equation and evaluates the refraction effects independently by using a ray tracing technique.

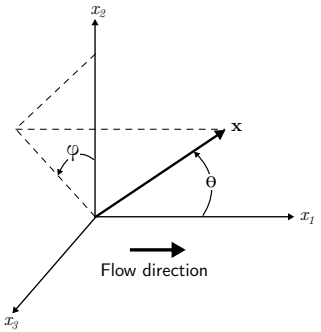

Figure 2.1 – Spherical and Cartesian coordinate systems.

2.2 LINEARIZED EULER EQUATIONS AS AN ACOUSTIC ANALOGY

Whereas the development showed in the previous section is derived from the complete Navier–Stokes equations, it is possible, as proposed by (MORRIS; FARASSAT, 2002; MORRIS; BOLURIAAN, 2004), for example, to start with the compressible, inviscid equations of motion for a perfect gas,

$$\frac{\partial \Pi}{\partial t} + U_j \frac{\partial \Pi}{\partial x_j} + \frac{\partial U_i}{\partial x_i} = 0\,, \tag{2.13}$$

$$\frac{\partial U_i}{\partial t} + U_j \frac{\partial U_i}{\partial x_j} + a^2 \frac{\partial \Pi}{\partial x_i} = 0\,, \tag{2.14}$$

where Π is the logarithmic pressure, defined as

$$\Pi \equiv \frac{1}{\gamma} \ln\left(\frac{p}{p_\infty}\right)\,, \tag{2.15}$$

with γ the ratio of specific heats and p_∞ a reference pressure defined at the observer position. Linearizing Equations 2.13 and 2.14 about a time-averaged state, the Linearized Euler Equations are obtained, which can be written as

$$\frac{\partial \Pi'}{\partial t} + \langle U_j \rangle \frac{\partial \Pi'}{\partial x_j} + \frac{\partial U_i'}{\partial x_i} = 0, \tag{2.16}$$

$$\frac{\partial U_i'}{\partial t} + \langle U_j \rangle \frac{\partial U_i'}{\partial x_j} + U_j' \frac{\partial \langle U_i \rangle}{\partial x_j} + \langle c \rangle^2 \frac{\partial \Pi'}{\partial x_i} = 0, \tag{2.17}$$

fully describing radiation of sound through a sheared flow.

It is possible to add terms in the right hand side of Equations 2.40 and 2.41 that relate to turbulent properties of the flow. These terms, as the right hand side of the Lighthill Equation (Equation 2.11), are then related to correlations evaluated from mean flow data. In this sense, the Linearized Euler Equations can be used as an acoustic analogy.

2.3 *TAM AND AURIAULT (1999)*

Tam and Auriault (1999) developed a method using the Linearized Euler Equations. The added source terms are related to a *turbulent pressure*. Based on an analogy with the kinetic theory of gases,

which relates the fluid pressure to the molecular velocity by

$$p \equiv \frac{1}{3}\rho \left\langle v_i v_i \right\rangle , \tag{2.18}$$

where v_i is the (i)th component of the molecular velocity vector, Tam and Auriault (1999) defined the instantaneous *turbulent pressure* as

$$p_{\text{turb}} \equiv \frac{1}{3}\rho u_i u_i. \tag{2.19}$$

Tam and Auriault (1999) write the momentum equations of the LEE, retaining on the right hand side terms related to the proposed turbulent pressure,

$$\langle\rho\rangle \left(\frac{\partial U_i'}{\partial t} + \langle U_j \rangle \frac{\partial U_i'}{\partial x_j} + U_j' \frac{\partial \langle U_i \rangle}{\partial x_j} \right) + \frac{\partial p'}{\partial x_i} = -\frac{\partial p_{\text{turb}}}{\partial x_i}, \tag{2.20}$$

where U_i' is the $(i)$the component of the velocity fluctuations related to sound waves. The authors also considered the linearized equations of energy and continuity. Next, the equations are written in a cylindrical polar coordinate system and the mean flow is assumed parallel.

Tam and Auriault (1999) proposed the solution of an equivalent adjoint problem instead of solving the inhomogeneous LEE. The pressure in the far field can be written as a function of the solution of the adjoint LEE as

$$p\left(\mathbf{y}, t\right) = \int_{-\infty}^{\infty}\int_{-\infty}^{\infty}\int_{-\infty}^{\infty}\int_{-\infty}^{\infty}\int_{-\infty}^{\infty} \left[\int_{-\infty}^{\infty} p_a\left(\mathbf{y}, \mathbf{x}, f\right) e^{-2\pi i f (t - t_1)} \mathrm{d}f \right] \frac{\mathrm{D}p_{\text{turb}}\left(\mathbf{x}, t_1\right)}{\mathrm{D}t_1} \mathrm{d}t_1 \mathrm{d}\mathbf{x}, \tag{2.21}$$

where p_a is the adjoint pressure and $^{\mathrm{D}}/_{\mathrm{D}t_1}$ is the material derivative.

After substitution of Equation (2.21) into Equation (2.4) and further mathematical manipulation, an equation for the acoustic pressure PSD is obtained:

$$\mathrm{S}\left(\mathbf{y}, f\right) = \int_{-\infty}^{\infty}\cdots\int_{-\infty}^{\infty} p_a\left(\mathbf{y}, \mathbf{x}_1, f_1\right) p_a\left(\mathbf{y}, \mathbf{x}_2, f_2\right) \left\langle \frac{\mathrm{D}p_{\text{turb}}\left(\mathbf{x}_1, t_1\right)}{\mathrm{D}t_1} \frac{\mathrm{D}p_{\text{turb}}\left(\mathbf{x}_2, t_2\right)}{\mathrm{D}t_2} \right\rangle e^{-2\pi i (f_1 + f_2) t + 2\pi i (f_1 t_1 + f_2 t_2)} \delta\left(f - f_2\right) \mathrm{d}f_1 \mathrm{d}f_2 \mathrm{d}t_1 \mathrm{d}t_2 \mathrm{d}\mathbf{x}_1 \mathrm{d}\mathbf{x}_2, \tag{2.22}$$

where $\mathbf{x}_1$ and $\mathbf{x}_2$ indicate two different source positions, t_1 and t_2 different time instants, and f_1 and f_2 different frequencies. As shown in Equation (2.22), S is a function of the space-time two-point au-

tocorrelation of the turbulent pressure material derivative. Based on experimental data for other turbulent correlations, Tam and Auriault (1999) proposed a model for the autocorrelation of the turbulent pressure material derivative,

$$\left\langle \frac{\mathrm{D}p_{\mathrm{turb}}\left(\mathbf{x}_1,t_1\right)}{\mathrm{D}t_1}\frac{\mathrm{D}p_{\mathrm{turb}}\left(\mathbf{x}_2,t_2\right)}{\mathrm{D}t_2}\right\rangle = \pi c_A^2 p_s^2 f_s^2 \exp\left\{-\frac{|\boldsymbol{\xi}|\, f_s}{\langle U_1\rangle}-\frac{\ln 2}{\ell_s^2}\left[\left(\xi_1-\langle U_1\rangle\,\tau\right)^2+\xi_2^2+\xi_3^2\right]\right\}, \tag{2.23}$$

where c_A is an empirical constant; p_s is a source characteristic turbulent pressure; f_s is a source characteristic frequency; ℓ_s is a source characteristic length scale; and $\boldsymbol{\xi}$ is the space separation vector.

Substitution of Equation (2.23) in Equation (2.22), and performing the integral in $\mathrm{d}\boldsymbol{\xi}$ along with further manipulation yields,

$$\mathrm{S}\left(\mathbf{y},f\right) = \pi^{5/2}4\iiint\limits_{V(\mathbf{x})}\left|p_a\left(\mathbf{y},\mathbf{x},f\right)\right|^2 c_A^2 p_s^2 \ell_s^3 f_s^2 \frac{1}{1+4\pi\left(f/f_s\right)^2}\exp\left[-\pi^2\left(\frac{f\ell_s}{\langle U_1\rangle}\right)^2\right]\mathrm{d}\mathbf{x}\,. \tag{2.24}$$

Morris and Farassat (2002) proposed that instead of solving the adjoint LEE, $\left|p_a\left(\mathbf{y},\mathbf{x},f\right)\right|^2$ should be obtained from the solution of the Helmholtz equation,

$$\frac{\partial p_a}{\partial x_i \partial x_i}+k^2 p_a = \frac{if}{a_\infty^2}\delta\left(\mathbf{x}-\mathbf{x}_2\right), \tag{2.25}$$

such that,

$$\left|p_a\left(r,f\right)\right|^2 = \frac{f^2}{16\pi^2 a_\infty^4 r^2}, \tag{2.26}$$

where the approximation $r\equiv|\mathbf{y}-\mathbf{x}|\approx|\mathbf{y}|$ is applied. With substitution of Equation (2.26) in Equation (2.24), the acoustic pressure PSD can be evaluated by

$$\mathrm{S}\left(r,f\right) = \frac{\sqrt{\pi}}{4\pi^2 a_\infty^4 r^2}\iiint\limits_{V(\mathrm{jet})} c_A^2 p_s^2 \ell_s^3 f_s^2 \frac{f^2}{1+4\pi\left(f/f_s\right)^2}\exp\left[-\pi^2\left(\frac{f\ell_s}{\langle U_1\rangle}\right)^2\right]\mathrm{d}V\,, \tag{2.27}$$

where $V\,(\mathrm{jet})$ is the volume of the RANS simulation domain.

The turbulent scales relate S to the RANS solution through the

following relations

$$p_s^2 = \frac{4}{9} c_A^2 \langle\rho\rangle^2 k,\ f_s = \frac{\varepsilon}{c_\tau k} \text{ and } \ell_s = c_\ell \frac{k^{3/2}}{\varepsilon} = \frac{c_\ell}{c_\tau} \frac{k^{1/2}}{f_s}, \tag{2.28}$$

where c_τ and c_ℓ are empirical constants, k is the mean turbulent kinetic energy per unit mass, and ε is the mean turbulent kinetic energy dissipation rate per unit mass. Along with c_A, c_τ and c_ℓ form the set of empirical constants used by *Tam and Auriault (1999)* method. These empirical constants are determined with a trial and error method, by comparison of the noise spectrum with experimental data. This process is carried independently for each set of constants used by the different methods.

The contribution from each infinitesimal fluid volume $\mathrm{d}V$ to the total acoustic pressure PSD is given by

$$\mathrm{dS}(r,f) = \frac{C}{r^2} \frac{c_A^2 c_\ell^3}{c_\tau^3} \langle\rho\rangle^2 k^{7/2} \frac{(f/f_s)^2}{1 + 4\pi^2 (f/f_s)^2} \exp\left[-\frac{\pi^2 c_\ell^2}{c_\tau^2} \frac{k}{\langle U_1 \rangle^2} \left(\frac{f}{f_s} \right)^2 \right] \mathrm{d}V, \tag{2.29}$$

where $\mathrm{d}V$ is approximated by the cell volume of the numerical RANS solution, and C is

$$C = \frac{\sqrt{\pi}}{9} \frac{1}{a_\infty^4}. \tag{2.30}$$

2.4 *MORRIS AND FARASSAT (2002)*

Morris and Farassat (2002) presented a comparison between the method of Tam and Auriault (1999) and a method derived from the Lighthill Equation.

Considering the observer at $\theta = 90°$, or $\mathbf{y} = (0, r, 0)$, and that $|\mathbf{y}| \gg |\mathbf{x}|$, the solution of Lighthill Equation (Equation (2.12)) is written as

$$\rho'(r,t) = \frac{1}{4\pi a_\infty^4} \frac{1}{r} \iiint\limits_{V(\mathbf{x})} \frac{\partial^2}{\partial t^2} T_{22} \left(\mathbf{x}, t - \frac{r}{a_\infty} \right) \mathrm{d}\mathbf{x}. \tag{2.31}$$

Next, the entropic term of the Lighthill stress tensor (Equation (2.10)) is discarded, which is valid for unheated jets. The viscous term is also discarded, narrowing the application to high-Reynolds-number jets. The inertial term is simplified to consider only turbulent fluctuations,

resulting in

$$T_{ij} \approx \langle \rho \rangle \, u_i u_j . \tag{2.32}$$

Using the relation $p' = a_\infty^2 \rho'$ and substituting ρ' given by Equation (2.31) into Equation (2.4), the acoustic pressure PSD can be written as

$$\mathrm{S}\left(r, f\right) = \frac{1}{16\pi a_\infty^4 r^2} \int_{-\infty}^{\infty} \iiint_{V(\mathbf{x}_2)} \iiint_{V(\mathbf{x}_1)} \left\langle \frac{\partial^2 T_{22}}{\partial t^2}\left(\mathbf{x}_1, t_1\right) \frac{\partial^2 T_{22}}{\partial t^2}\left(\mathbf{x}_2, t_2\right) \right\rangle \mathrm{d}\mathbf{x}_1 \mathrm{d}\mathbf{x}_2 e^{2\pi i f \tau} \mathrm{d}\tau \, . \tag{2.33}$$

Assuming statistically stationary turbulence, it is possible to write

$$\begin{aligned} \left\langle \frac{\partial^2 T_{22}}{\partial t^2}\left(\mathbf{x}_1, t_1\right) \frac{\partial^2 T_{22}}{\partial t^2}\left(\mathbf{x}_2, t_2\right) \right\rangle &= \frac{\partial^4}{\partial \tau^4} \left\langle T_{22}\left(\mathbf{x}_1, t_1\right) T_{22}\left(\mathbf{x}_2, t_2\right) \right\rangle \\ &= \frac{\partial^4}{\partial \tau^4} R_{T_{22}T_{22}}\left(\mathbf{x}, \boldsymbol{\xi}, \tau\right) , \end{aligned} \tag{2.34}$$

where $R_{T_{22}T_{22}}\left(\mathbf{x}, \boldsymbol{\xi}, \tau\right)$ is the space-time two-point autocorrelation of the approximated Lighthill stress tensor (GOLDSTEIN, 1976). The autocorrelation is modeled by

$$R_{T_{22}T_{22}}\left(\mathbf{x}, \boldsymbol{\xi}, \tau\right) = c_A^2 \left\langle \rho \right\rangle^2 u_s^4 \exp\left(-\frac{\left|\boldsymbol{\xi}\right|^2}{\ell_s^2} - f_s^2 \tau^2 \right) , \tag{2.35}$$

where u_s is a source characteristic turbulent velocity.

After Equations (2.34) and (2.35) are substituted into Equation (2.33), integrated over $\mathrm{d}\boldsymbol{\xi}$, Fourier-transformed, and further simplified, the PSD can be evaluated by the following volume integral,

$$\mathrm{S}\left(r, f\right) = \frac{c_A^2 \pi^3}{2 a_\infty^4 r^2} \iiint_{V(\mathrm{jet})} \left\langle \rho \right\rangle^2 u_s^4 \ell_s^3 f_s^3 \left(\frac{f}{f_s} \right)^4 \exp\left[-\pi^2 \left(\frac{f}{f_s} \right)^2 \right] \mathrm{d}V \, . \tag{2.36}$$

The source scales in Equation (2.36) are related to the RANS solution as follows:

$$u_s = \sqrt{\frac{2k}{3}}, \; f_s = \frac{\varepsilon}{c_\tau k} \;\text{ and }\; \ell_s = c_\ell \frac{k^{3/2}}{\varepsilon} = \frac{c_\ell}{c_\tau} \frac{k^{1/2}}{f_s} ; \tag{2.37}$$

where c_l and c_τ are empirical constants. The elemental contribution to

the total PSD is

$$\mathrm{dS}\left(r,f\right)=\frac{C}{r^2}\frac{c_A^2c_\ell^3}{c_\tau^3}\left\langle\rho\right\rangle^{\,2}k^{7/2}\left(\frac{f}{f_s}\right)^4\exp\left[-\pi^2\left(\frac{f}{f_s}\right)^2\right]\mathrm{d}V, \tag{2.38}$$

with

$$C=\frac{\pi^2}{9}\frac{1}{a_\infty^4}. \tag{2.39}$$

2.5 *MORRIS AND BOLURIAAN (2004)*

Morris and Boluriaan (2004) followed the work of Morris and Farassat (2002) and proposed a method similar to that of *Tam and Auriault (1999)*, however without resorting to an analogy with the kinetic theory of gases. The *Morris and Boluriaan (2004)* formulation can consider sound-flow interaction effects. A simplified formulation that was derived by the authors for an observer at $\theta = 90°$ is adopted in this dissertation.

Starting from the Linearized Euler Equations, as presented in Section 2.2, Morris and Boluriaan (2004) add source terms represented by Θ and F_i in the mass and momentum equations, respectively. Thus, the resulting equation can be written as

$$\frac{\partial\Pi'}{\partial t}+\left\langle U_j\right\rangle\frac{\partial\Pi'}{\partial x_j}+\frac{\partial U_i'}{\partial x_i}=\Theta, \tag{2.40}$$

$$\frac{\partial U_i'}{\partial t}+\left\langle U_j\right\rangle\frac{\partial U_i'}{\partial x_j}+U_j'\frac{\partial\left\langle U_i\right\rangle}{\partial x_j}+\left\langle c\right\rangle^2\frac{\partial\Pi'}{\partial x_i}=F_i, \tag{2.41}$$

which fully describe the generation and radiation of sound from a turbulent flow with non-homogeneous mean velocity and speed of sound.

The fluctuations in the logarithmic pressure are approximated by

$$\Pi'\approx\frac{p'}{\gamma p_\infty}\,. \tag{2.42}$$

Solving Equations (2.40) and (2.41) by the use of the appropriate

Green's functions, the pressure fluctuation can be written as

$$p'(\mathbf{y},t) = \gamma p_\infty \int_{-\infty}^{\infty}\!\!\int_{-\infty}^{\infty}\!\!\int \int_{-\infty}^{\infty} \Pi_g^0(\mathbf{y},t\,|\mathbf{x},\tau)\,\theta(\mathbf{x},\tau) + \sum_{n=1}^{3} \Pi_g^n(\mathbf{y},t\,|\mathbf{x},\tau)\,F_n(\mathbf{x},\tau)\,\mathrm{d}\tau\mathrm{d}\mathbf{x}\,, \tag{2.43}$$

where $\Pi_g^{n=0\ldots3}$ are the four Green's functions for Π. For the case of an observer at 90° to the jet axis, only $\Pi_g^{n=0}$ and $\Pi_g^{n=2}$ are relevant. It can be shown that the results for $n=0$ and $n=2$ only differ by a constant factor, which can be adjusted via calibrated empirical constants. Thus, only the derivation for $n=2$ is presented hereafter.

By using Equation (2.43), the pressure autocorrelation can be written as

$$\begin{aligned}\langle p'(\mathbf{y},t)\,p'(\mathbf{y},t+\tau)\rangle = {}& \frac{\rho_\infty^2 a_\infty^4}{4\pi^2} \int_{-\infty}^{\infty}\!\!\cdots\!\!\int \Pi_g^2(\mathbf{y}\,|\mathbf{x}_1,f_1)\,\Pi_g^2(\mathbf{y}\,|\mathbf{x}_2,f_2)\,\langle F_2(\mathbf{x}_1,\tau_1)\,F_2(\mathbf{x}_2,\tau_2)\rangle \\ & \exp\left[-2\pi i f_1(t-\tau_1)\right]\exp\left[-2\pi i f_2(t-\tau_2)-2\pi i f_2\tau\right] \\ & \mathrm{d}f_1\mathrm{d}f_2\mathrm{d}\tau_1\mathrm{d}\tau_2\mathrm{d}\mathbf{x}_1\mathrm{d}\mathbf{x}_2\,,\end{aligned} \tag{2.44}$$

which is a function of the space-time two-point autocorrelation of the momentum source term in the x_2 direction, F_2. Based on available measurements of turbulence statistics, the autocorrelation for F_2 is modeled as

$$\langle F_2(\mathbf{x}_1,\tau_1)\,F_2(\mathbf{x}_2,\tau_2)\rangle = c_A^2 \frac{u_s^6}{a_\infty^2 \ell_1^2} \exp\left[-|\tau|\,f_s - \frac{(\xi_1-\langle U_1\rangle\tau)^2+\xi_2^2+\xi_3^2}{\ell_s^2}\right]. \tag{2.45}$$

For an observer at 90° to the jet axis, Π_g^2 takes the form

$$\left|\Pi_g^2(r,f)\right|^2 = \frac{f}{4a_\infty^6 r^2}\,. \tag{2.46}$$

The characteristic source scales are related to the RANS solution as

$$u_s = \sqrt{\frac{2}{3}k}\,,\quad f_s = \frac{\varepsilon}{c_\tau k}\ \ and\ \ \ell_s = c_\ell \frac{k^{3/2}}{\varepsilon} = \frac{c_\ell}{c_\tau}\frac{k^{1/2}}{f_s}\,, \tag{2.47}$$

where c_τ and c_ℓ are empirical constants.

Using Equations (2.47), (2.46), (2.45) and (2.44) in Equation

(2.4), the spectral density can be written as

$$\mathrm{S}\left(r,f\right)=\frac{4\pi^{3/2}}{27}c_A^2\left(\frac{c_l}{c_\tau}\right)\frac{\rho_\infty^2}{a_\infty^4 r^2}\iiint\limits_{V(\mathrm{jet})}k^{7/2}\frac{\left(f/f_s\right)^2}{1+4\pi^2\left(f/f_s\right)^2}\exp\left[-\pi^2\left(\frac{c_l}{c_\tau}\right)^2\frac{k}{a_\infty^2}\left(\frac{f}{f_s}\right)^2\right]\mathrm{d}V. \quad (2.48)$$

Hence, the elemental contribution to the spectral density can be written as

$$\mathrm{dS}\left(r,f\right)=\frac{C}{r^2}c_A^2\left(\frac{c_l}{c_\tau}\right)k^{7/2}\frac{\left(f/f_s\right)^2}{1+4\pi^2\left(f/f_s\right)^2}\exp\left[-\pi^2\left(\frac{c_l}{c_\tau}\right)^2\frac{k}{a_\infty^2}\left(\frac{f}{f_s}\right)^2\right]\mathrm{d}V, \quad (2.49)$$

with

$$C=\frac{4\pi^{3/2}}{27}\frac{\rho_\infty^2}{a_\infty^4}. \quad (2.50)$$

2.6 *LRT (2011)*

The source model presented by Ilário (2011) to predict jet noise is based on the Lighthill Equation and the new time scale presented by Azarpeyvand (2008). It can be shown that the derivation is similar to that of *Morris and Farassat (2002)* method up to Equation (2.35).

The *LRT (2011)* method adopts a different model for the turbulent velocity correlation. Instead of modelling the fourth-order correlation,

$$\left\langle u_i u_j u_k u_l\right\rangle, \quad (2.51)$$

by a Gaussian function like in *Morris and Farassat (2002)*, such a correlation is expressed in terms of second-order correlations, such as

$$\left\langle u_i u_j\right\rangle\left\langle u_k u_l\right\rangle, \quad (2.52)$$

and finally each second-order correlation is independently modelled by a Gaussian function. This yields a different exponential argument, as a result of performing the Fourier transform of $\left[\exp\left(-\tau^2 f_s^2\right)^2\right]$ instead of $\left[\exp\left(-\tau^2 f_s^2\right)\right]$.

After integrating over $\mathrm{d}\boldsymbol{\xi}$ and taking the Fourier transform, the

resulting model for the fourth-order correlation is

$$R_{T_{22}T_{22}}(\mathbf{y}, f) = \langle\rho\rangle^2 u_s^4 \ell_s^3 \left(\frac{f}{f_s}\right)^4 \exp\left[-\frac{\pi^2}{2}\left(\frac{f}{f_s}\right)^2\right]. \tag{2.53}$$

Following the same procedure used by *Morris and Farassat (2002)* method, the acoustic pressure PSD is given by

$$\mathrm{S}(r, f) = \frac{\pi^{1/2}}{4}\frac{1}{a_\infty^4 r^2}\iiint\limits_{V(\mathrm{jet})} \langle\rho\rangle^2 u_s^4 \ell_s^3 \left(\frac{f}{f_s}\right)^4 \exp\left[-\frac{\pi^2}{2}\left(\frac{f}{f_s}\right)^2\right] \mathrm{d}V. \tag{2.54}$$

The source scales are evaluated from the RANS solution through the following relations:

$$u_s = \sqrt{k},\ f_s = \frac{\mathrm{D}_{\mathrm{jet}}^{2/3}}{c_\tau c_\ell^{2/3}}\frac{\varepsilon^{5/3}}{k^2} \ \text{ and } \ \ell_s = \frac{c_\ell}{c_\tau}\frac{k^{1/2}}{f_s}, \tag{2.55}$$

where c_l and c_τ are empirical constants and $\mathrm{D}_{\mathrm{jet}}$ is the nozzle diameter.

The source characteristic frequency in Equation (2.55) uses the time scale proposed by Azarpeyvand (2008), which is based on the turbulent energy transfer (TET) rate instead of the usual turbulent dissipation rate. With the source scales from Equation (2.55) introduced into Equation (2.54), the elemental contribution to the PSD is

$$\mathrm{dS}(r, f) = \frac{C}{r^2}\frac{c_\ell^3}{c_\tau^3}\langle\rho\rangle^2 k^{7/2}\left(\frac{f}{f_s}\right)^4 \exp\left[-\frac{\pi^2}{2}\left(\frac{f}{f_s}\right)^2\right] \mathrm{d}V, \tag{2.56}$$

with

$$C = \frac{\pi^{5/2}}{4}\frac{1}{a_\infty^4}. \tag{2.57}$$

2.7 SUMMARY OF FINAL EQUATIONS

Table 2.1 presents the characteristic source frequency definition and the final equations for the RANS-based methods. The characteristic source frequency relates the inverse of the local turbulent time scale to the generation of sound. The *LRT (2011)* approach uses a different definition of the characteristic source frequency, which is the most important difference in relation to the *Morris and Farassat (2002)* method.

The frequency dependence of the methods based on the Lighthill Equation, *Morris and Farassat (2002)* and *LRT (2011)*, are identical.

This is also the case with the methods based on the Linearized Euler Equations, *Tam and Auriault (1999)* and *Morris and Boluriaan (2004)*. Both methods based on the LEE carry information about the velocity in the exponential argument, which is a consequence of the relation used to model the autocorrelation of the source terms.

Table 2.1 – Summary of final equations.

Method	Characteristic source frequency, f_s	Elemental contribution, ${}^{\mathrm{d}S r^2}/_{C\mathrm{d}V}$
Tam and Auriault (1999)	$\dfrac{\varepsilon}{c_\tau k}$	$\dfrac{c_A^2 c_\ell^3}{c_\tau^3}\left\langle\rho\right\rangle^2 k^{7/2}\dfrac{\left(f/f_s\right)^2}{1+4\pi^2\left(f/f_s\right)^2}\exp\left[-\dfrac{\pi^2 c_\ell^2}{c_\tau^2}\dfrac{k}{\left\langle U_1\right\rangle^2}\left(\dfrac{f}{f_s}\right)^2\right]$
Morris and Farassat (2002)	$\dfrac{\varepsilon}{c_\tau k}$	$\dfrac{c_A^2 c_\ell^3}{c_\tau^3}\left\langle\rho\right\rangle^2 k^{7/2}\left(\dfrac{f}{f_s}\right)^4\exp\left[-\pi^2\left(\dfrac{f}{f_s}\right)^2\right]$
Morris and Boluriaan (2004)	$\dfrac{\varepsilon}{c_\tau k}$	$\dfrac{c_A^2 c_\ell}{c_\tau}k^{7/2}\dfrac{\left(f/f_s\right)^2}{1+4\pi^2\left(f/f_s\right)^2}\exp\left[-\dfrac{\pi^2 c_\ell^2}{c_\tau^2}\dfrac{k}{a_\infty^2}\left(\dfrac{f}{f_s}\right)^2\right]$
LRT (2011)	$\dfrac{\mathrm{D}_{\mathrm{jet}}^{2/3}\varepsilon^{5/3}}{c_\tau c_\ell^{2/3}k^2}$	$\dfrac{c_\ell^3}{c_\tau^3}\left\langle\rho\right\rangle^2 k^{7/2}\left(\dfrac{f}{f_s}\right)^4\exp\left[-\dfrac{\pi^2}{2}\left(\dfrac{f}{f_s}\right)^2\right]$

2.8 SCALING OF MAXIMUM SPL AND PEAK FREQUENCY

Although the methods presented in the previous sections are mainly used to calculate noise spectra, it is possible to derive scaling relations using their final equations. Table 2.1 shows that the source models result in

$$S \propto k^{7/2}, \tag{2.58}$$

which results in the SPL also scaling with $k^{7/2}$. A coefficient related to $k^{7/2}$ can be defined as

$$C_{k^{7/2}} \equiv \iiint\limits_{V(\text{jet})} k^{7/2} \mathrm{d}V, \tag{2.59}$$

which gives information about the distribution of $k^{7/2}$ for a given jet. $C_{k^{7/2}}$ can be expressed in dB scale by

$$C^{\text{dB}}_{k^{7/2}} = 10 \log_{10} C_{k^{7/2}}. \tag{2.60}$$

The dependence with frequency differs between the methods, only *LRT (2011)* method is chosen to evaluate the peak frequency. It will be shown in later chapters that *LRT (2011)* is considered the most suitable source model, thus motivating its choice for a study on the peak frequency. By setting

$$\frac{\mathrm{d}\,(\mathrm{dS})}{\mathrm{d}f} = 0, \tag{2.61}$$

it can be shown that the peak frequency for each point in the domain is

$$\frac{f_s}{\pi}. \tag{2.62}$$

A weighted-average, given by

$$f_{\text{peak}} = \frac{\iiint\limits_{V(\text{jet})} \frac{f_s}{\pi} k^{7/2} \mathrm{d}V}{\iiint\limits_{V(\text{jet})} k^{7/2} \mathrm{d}V}, \tag{2.63}$$

is used to evaluate the effective peak frequency representing the entire jet.

3 RAY TRACING METHOD

Ilário (2011) implemented a method based on classical ray acoustics theory (PIERCE, 1981) to supplement the source modelling in *LRT (2011)*. Ray acoustics is a well-established theory to analyse sound propagation in classical acoustics, having few applications in aeroacoustics.

Freund and Fleischman (2002) used DNS data and a ray tracing method to investigate the transient effects of turbulence in the propagation of sound through a turbulent jet. They showed that rays traced through the transient flow result in a different directivity from that of rays traced through the mean flow. Conversely, Spalart, Shur and Strelets (2007) showed that tracing the rays through the mean flow yielded results in good agreement with their LES and experimental data. Ilário (2011) also considered the mean flow, validating the ray tracing results with experiments for several nozzle configurations and operating conditions.

This chapter describes the three-dimensional ray tracing method implemented by Ilário (2011), which is based on the derivation presented by Pierce (1981). The ray tracing method is subsequently used to evaluate the effect of sound-flow interaction on sound emitted from monopole sources within different jets. The method gives the paths of the refracted rays and the corresponding change in sound pressure level (ΔSPL).

3.1 RAY TRACING EQUATIONS

The derivation of the ray tracing equations is based on vector calculus and the concepts of wavefront, ray path and wave-slowness vector. The wavefront, shown in Figure 3.1, defines a surface where the pressure fluctuations are in phase at a given time $\Omega(\mathbf{x}) = t$. Let $\mathbf{x}_{\text{ray}}(t)$ be a point on the wavefront defining the position of a ray at instant t. The point follows the wavefront with velocity

$$\mathbf{V}_{\text{ray}} \equiv \frac{\mathrm{d}\mathbf{x}_{\text{ray}}}{\mathrm{d}t} = \langle \mathbf{U} \rangle + \langle a \rangle \, \mathbf{n}, \tag{3.1}$$

where $\mathbf{n}$ is a unit vector normal to the wavefront. It is possible to calculate the ray path by integrating Equation (3.1) in time, given $\langle \mathbf{U} \rangle$, $\langle c \rangle$, and $\mathbf{n}$. However, the evaluation of $\mathbf{n}$ requires the reconstruction of the wavefront at each time step, which in turn requires the position of all neighboring rays. Instead of doing this, it is proposed to define the wave-slowness vector, $\mathbf{s}$, with components

$$s_i \equiv \frac{\partial \Omega}{\partial x_i}. \tag{3.2}$$

It can be shown that $\mathbf{s}$ is parallel to $\mathbf{n}$, so instead of recreating the wavefront at each time step to calculate $\mathbf{n}$, it is possible to use $\mathbf{s}$.

Resorting to geometrical reasoning and vector calculus, a differential equation for $\mathbf{s}$ is proposed, and the ray tracing equations are written as (PIERCE, 1981)

$$\frac{\mathrm{d}x_{\mathrm{ray},i}}{\mathrm{dt}} = \langle U_i \rangle + \frac{\langle a \rangle^2 s_i}{1 - \langle U_j \rangle s_j} \tag{3.3}$$

and

$$\frac{\mathrm{d}s_i}{\mathrm{dt}} = -\frac{1 - \langle U_j \rangle s_j}{\langle a \rangle} \frac{\partial \langle a \rangle}{\partial x_i} - s_j \frac{\partial \langle U_j \rangle}{\partial x_i}. \tag{3.4}$$

Equations (3.3) and (3.4) are solved as an initial value problem by a fourth-order Runge-Kutta method (PRESS et al., 1997). The mean flow properties, $\langle \mathbf{U} \rangle$ and $\langle a \rangle$, are interpolated from a RANS solution by using a trilinear interpolation method.

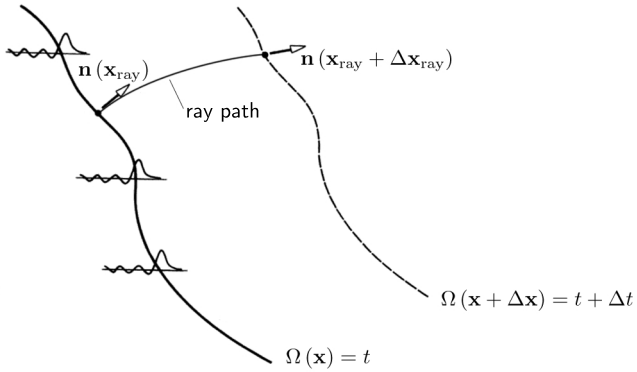

Figure 3.1 – Wavefront surface concept. The wavefront is defined by all points $\mathbf{x}$ that have the same wave feature at time τ. The ray path can be described by following a single ray from $\mathbf{x}_{\mathrm{ray}}$ to $\mathbf{x}_{\mathrm{ray}} + \Delta\mathbf{x}_{\mathrm{ray}}$. Adapted from (PIERCE, 1981).

3.2 MODELLING A MONOPOLE SOURCE

To quantify the effects of refraction on the sound emitted from monopole sources, Equations (3.3) and (3.4) are solved for a large number of rays (over 10^5) up to the time when each ray reaches a distance of around $100D_{jet}$ from the nozzle exit, which is considered to be located in the acoustic far field. The monopole source is chosen because it radiates sound equally in all directions. Hence, it is possible to isolate the effect of refraction on the directivity. To properly emulate the directivity of a monopole, the rays should be emitted in evenly distributed angles around a sphere circumscribing the source position. Such uniformity can be exactly achieved by using the vertices of a regular polyhedron. However, as no regular polyhedron has more than twenty vertices, the vertices of a geodesic sphere can be used (PATWARI; DURGIN; RAPPAPORT, 1997).

The geodesic sphere can be generated by recursively dividing the faces of an initial icosahedron until the desired number of vertices is achieved. Figure 3.2 shows an example of a geodesic sphere generated by this procedure. A geodesic sphere centered at the nozzle exit is also used to define a number of far field areas (over 10^4) where ΔSPL is calculated.

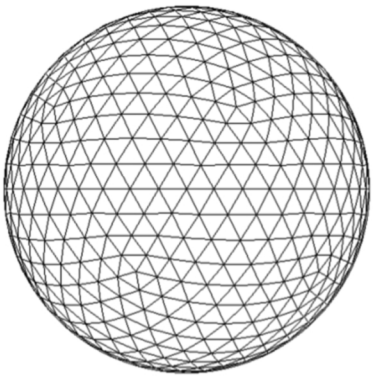

Figure 3.2 – Geodesic sphere formed by the recursive division of the faces of a regular icosahedron. The emission angles are defined at the vertices of the geodesic. Extracted from (PATWARI; DURGIN; RAPPAPORT, 1997).

3.3 ΔSPL EVALUATION

As the ray tracing equations, Equations (3.3) and (3.4), do not carry information about the acoustic pressure amplitude along the ray path, an indirect calculation is needed. The concept of ray tubes and the principle of conservation of energy lead to the definition of the Blokhintzev invariant, which can be used to analyse relative changes of acoustic pressure amplitude along the ray path (PIERCE, 1981). It follows that

$$\frac{P^2 \left|\mathbf{V}_{ray}\right| A}{\left(1 - \langle U_i \rangle \, s_i\right) \langle \rho \rangle \, \langle a \rangle^2} = \text{const}, \tag{3.5}$$

where P is the acoustic pressure amplitude and A is the ray tube area. By using Equation (3.5), the relative change of acoustic pressure amplitude between the source position and the far field observer position can be calculated by

$$\frac{P^2\big|_{\text{far field}}}{P^2\big|_{\text{source}}} = \frac{\left.\frac{\left|\mathbf{V}_{\text{ray}}\right|}{\left(1-\langle U_i\rangle s_i\right)\langle\rho\rangle\langle a\rangle^2}\right|_{\text{source}}}{\left.\frac{\left|\mathbf{V}_{\text{ray}}\right|}{\left(1-\langle U_i\rangle s_i\right)\langle\rho\rangle\langle a\rangle^2}\right|_{\text{far field}}} \; \frac{A\big|_{\text{source}}}{A\big|_{\text{far field}}}, \tag{3.6}$$

where the position at which the properties are calculated is indicated. The first term on the right hand side of Equation (3.6) is evaluated in a straightforward manner using the ray tracing solution and the information interpolated from the RANS solution. The area ratio, however, requires special treatment.

In Equation (3.6), the area ratio also takes into account the amplitude drop caused by the spherical spreading of sound emitted from a monopole source. As the spherical spreading is already considered by the source models ($S \propto 1/r^2$), the area ratio in Equation (3.6) is replaced by the area ratio of the ray tubes in the far field without and with refraction effects. The new ratio is given by

$$\frac{A\big|_{\text{non-refracted}}}{A\big|_{\text{refracted}}}. \tag{3.7}$$

Furthermore, the ray tube areas are approximated by the ray density, which is calculated by counting the rays crossing each far field area, as depicted in Figure 3.3. First, the number of rays crossing each area is calculated without solving the ray tracing equations as $N_{\text{non-refracted}}$ (all rays following a straight line from the source). Second, the far field position of the refracted rays are calculated by the solution of the ray tracing equations and the number of rays crossing each area

is calculated as $N_{\text{refracted}}$. Thus, Equation (3.6) is rewritten so the amplitude change caused by refraction can be assessed by

$$\frac{P^2\big|_{\text{refracted}}}{P^2\big|_{\text{non-refracted}}} = \frac{\left.\frac{|\mathbf{v}_{\text{ray}}|}{(1-\langle U_i\rangle s_i)\langle\rho\rangle\langle a\rangle^2}\right|_{\text{source}}}{\left.\frac{|\mathbf{v}_{\text{ray}}|}{(1-\langle U_i\rangle s_i)\langle\rho\rangle\langle a\rangle^2}\right|_{\text{far field}}} \frac{N\big|_{\text{refracted}}}{N\big|_{\text{non-refracted}}}. \tag{3.8}$$

Finally, the change in sound pressure level caused by refraction can be calculated for each far field area by

$$\Delta\text{SPL} = 10\log_{10}\left(\frac{P^2_{\text{refracted}}}{P^2_{\text{non-refracted}}}\right). \tag{3.9}$$

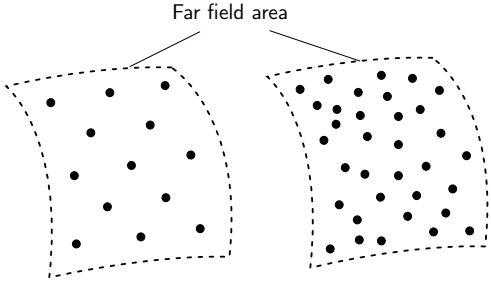

Figure 3.3 – Representation of rays crossing a far field area. The higher number of dots in (b) represents an amplification caused by refraction. It is emphasized in (a) how the non-refracted rays are equally spaced, which is not necessarily the case for refracted rays as shown in (b).

4 RESULTS

In order to study aspects of jet noise, the methods described in Chapters 2 and 3 are used along with results from RANS simulations carried out by Ilário (2011) and Engel (2012) (more information about the RANS simulations can be found in Appendix A). Figure 4.1 and Table 4.1 show information about the cases that are considered, which cover five nozzle geometries and eight operating conditions. The results are grouped according to main aspects of the jet flow: cold or hot jets issued from the single-stream or dual-stream nozzles, and cold jets issued from chevron nozzles. Moreover, Figure 4.2 shows the positions of sound sources used for the refraction analysis with the ray tracing technique.

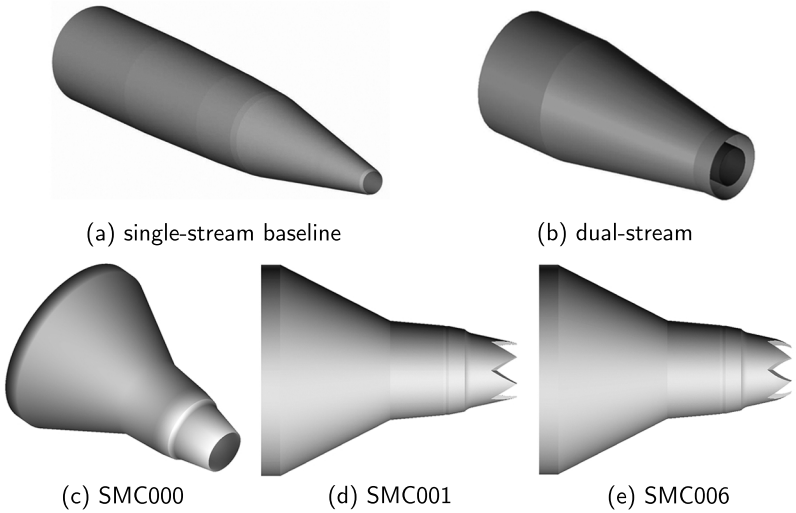

Figure 4.1 – Nozzle geometries.

Table 4.1 – Cases information.

Case	Nozzle designation	Diameter [m]	M_{jet}	TR[a]	r	Experimental data	RANS simulation
1	single-stream baseline	0.1016	0.50	1.00	1 m[e]	(ILáRIO, 2011)	(ILáRIO, 2011)
2	single-stream baseline	0.1016	0.75	1.00			
3	single-stream baseline	0.1016	1.00	1.00			
4	single-stream baseline	0.1016	0.50	2.00			
5	single-stream baseline	0.1016	0.75	2.00			
6	dual-stream	0.033[b], 0.058[c]	0.84[b], 0.50[c]	1.00	6 m[f]	(ILáRIO, 2011)	(ILáRIO, 2011)
7	dual-stream	0.033[b], 0.058[b]	0.84[b], 0.84[c]	1.00			
8	SMC000	0.0508	0.90	0.86	$40D_{jet}$[g]	(BRIDGES; BROWN, 2004)	(ENGEL, 2012)
9	SMC001	0.0522[d]	0.90	0.86			
10	SMC006	0.0477[d]	0.90	0.86			

[a] Temperature Ratio, defined by the ratio of the temperature at the nozzle exit and the temperature at the observer position.
[b] Primary stream.
[c] Secondary stream.
[d] Equivalent diameter based on the mass flow rate (BRIDGES; BROWN, 2004).
[e] Measured at 12 m, adjusted to 1 m.
[f] Measured at 12 m, adjusted to 6 m.
[g] Measured at 2.54 m, adjusted to $40D_{jet}$.

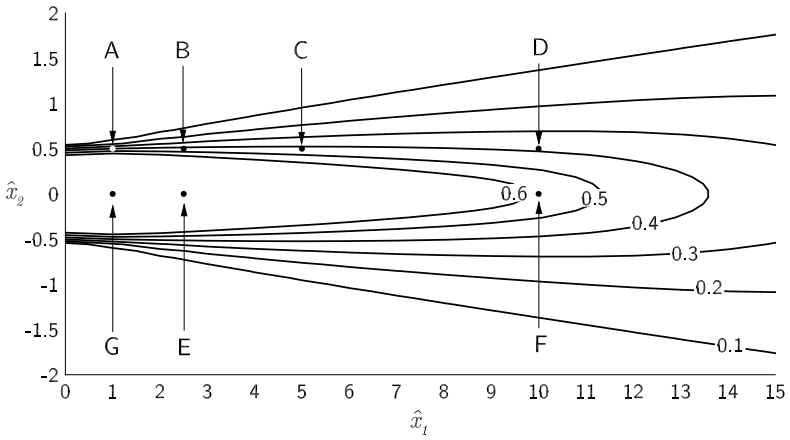

Figure 4.2 – Normalized source positions (A–G) and lines of constant $\langle U_1 \rangle / c_\infty$ for a cold single-stream jet (*Case 2*). The spatial coordinates, $\hat{x}_i$, are normalized by the nozzle diameter as $\hat{x}_i \equiv x_i / D_{\text{jet}}$.

4.1 EMPIRICAL CONSTANTS

Table 4.2 shows that the source models rely on empirical constants that had to be calibrated for the majority of cases. The calibration follows a trial and error procedure, in which the SPL is iteratively computed until a reasonable accuracy is found by a visual comparison of the numerical SPL curve with experimental data. The computational code used to compute the SPL is presented in Appendix B.

The fact that, for each method, the constants remained unchanged for *Cases 1*, *2*, and *3*, is an evidence that the source models capture well the mechanisms of sound generation in single-stream cold jets with Mach numbers in the range 0.50–1.00. However, for the remaining cases the prediction methods do not take into account all the physical phenomena involved in the generation of jet noise.

Table 4.2 – Empirical constants used by the source strength models.

Case	*Tam and Auriault (1999)*			*Morris and Farassat (2002)*		*Morris and Boluriaan (2004)*			*LRT (2011)*	
	A	c_ℓ	c_τ	$A^2 c_\ell^3$	c_τ	B	c_ℓ	c_τ	c_ℓ	c_τ
1	8.0	0.2	0.2	1.0	0.255	1.7	0.8	0.12	0.8	0.45
2	8.0	0.2	0.2	1.0	0.255	1.7	0.8	0.12	0.8	0.45
3	8.0	0.2	0.2	1.0	0.255	1.7	0.8	0.12	0.8	0.45
4	10.4	0.35	0.2	11.2	0.3	4.8	1.2	0.8	1.5	0.46
5	4.6	0.35	0.15	3.6	0.3	2.2	0.8	0.26	1.0	0.45
6	1.8	0.1	0.04	0.024	0.092	1.2	0.3	0.03	0.34	0.28
7	0.08	0.12	0.00018	0.0052	0.05	1.7	0.12	0.026	0.25	0.16
8	2.56	0.09	0.009	0.064	0.05	7.84	0.07	0.05	0.4	0.12
9	3.12	0.047	0.0047	0.0064	0.02	8.22	0.045	0.02	0.26	0.065
10	2.2	0.04	0.002	0.004	0.016	7.4	0.05	0.005	0.22	0.05

4.2 COLD JETS

Cold single-stream jets are rarely present in engineering problems, and definitely not present in the problem of aircraft noise. Nevertheless, it is a flow condition frequently adopted to study the fundamentals of noise generation and to assess noise prediction methods. Section 4.2.1 presents results for acoustic noise generated by cold single-stream jets at different Mach numbers, followed by an analysis of sound refraction and the effect of the turbulent energy transfer (TET) time scale in Sections 4.2.2 and 4.2.3, respectively.

4.2.1 Mach number

In Section 2.8, it was shown that the studied source strength models indicate that the sound pressure level scales with $k^{7/2}$ and a relation to evaluate the peak frequency was presented. In Table 4.3 it is indicated how $C^{\mathrm{dB}}_{k^{7/2}}$ (see Equation (2.60)) and the experimental maximum SPL increases between *Cases 1–2* and between *Cases 2–3*. As can be seen, the changes in $C^{\mathrm{dB}}_{k^{7/2}}$, which is independent of the chosen source strength model, agree well with the changes of the experimental maximum SPL.

Table 4.3 – Increase of $C^{\mathrm{dB}}_{k^{7/2}}$ and experimental maximum SPL between cold single-stream jets.

Cases	$C^{\mathrm{dB}}_{k^{7/2}}$	Experimental maximum SPL
1–2	12.2 dB	11.2 dB
2–3	8.5 dB	8.6 dB

Table 4.4 shows the comparison of the experimental peak frequency with the peak frequency calculated with Equation (2.63), which was derived from *LRT (2011)* method. Although there is significant error between the values, the trend of an increasing peak frequency with Mach number is captured. The error can be caused by the flatness of the spectra near the peak frequency and poor calibration of the constants.

Finally, Figure 4.3 summarizes the experimentally verified effect

Table 4.4 – Peak frequency evaluation for cold single-stream jets (*Cases 1*, *2*, and *3*).

Case	Numerical f_{peak}	Experimental f_{peak}
1	620.4 Hz	489.4 Hz
2	846.2 Hz	725.0 Hz
3	1288.4 Hz	917.4 Hz

of Mach number on noise emitted from cold single-stream jets along with the corresponding numerical predictions. The numerical results in Figure 4.3 are computed with the empirical constants established for the case with $M_{\text{jet}} = 0.75$. The *Tam and Auriault (1999)* and *LRT (2011)* methods predict well the noise spectra, which confirms the presented analyses for maximum SPL and peak frequency.

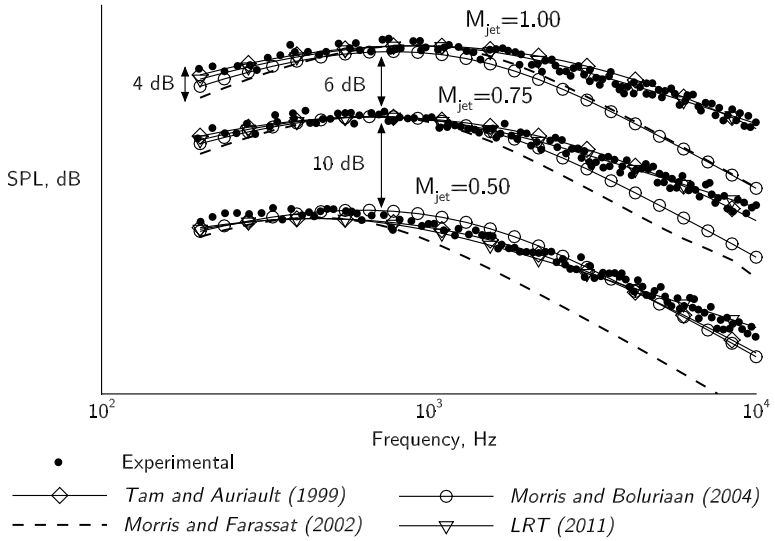

Figure 4.3 – SPL for cold single-stream jets (*Cases 1*, *2*, and *3*). Mach number effect on the emitted noise. Experimental data from (ILáRIO, 2011).

Only a relative scale for SPL is shown in Figure 4.3. This is

done to emphasize the objective of the plot, which is not to analyse the maximum SPL, but to compare the shape of the numerical spectra with experimental results. Moreover, the maximum SPL varies with the distance from the nozzle exit, which in turn would add more complexity to the analysis instead of making it more clear. The remaining SPL plots in this dissertation also follow this motivation.

4.2.2 Source position

Contrary to the usual delimitation of the zone of silence by a single critical angle, it can be shown that the critical angle is a function of the source position for a given jet. With this purpose, the ray tracing method presented in Chapter 3 is used to evaluate the refraction in a cold single-stream jet (*Case 2*). Among the studied source positions (Figure 4.2), the greatest difference was found to be approximatelly 6° between the critical angles for source positions B and D. Figure 4.4 shows contour plots of ΔSPL used to estimate the critical angles. The coloured regions indicate an amplification or attenuation caused by refraction and the white regions indicate the zone of silence.

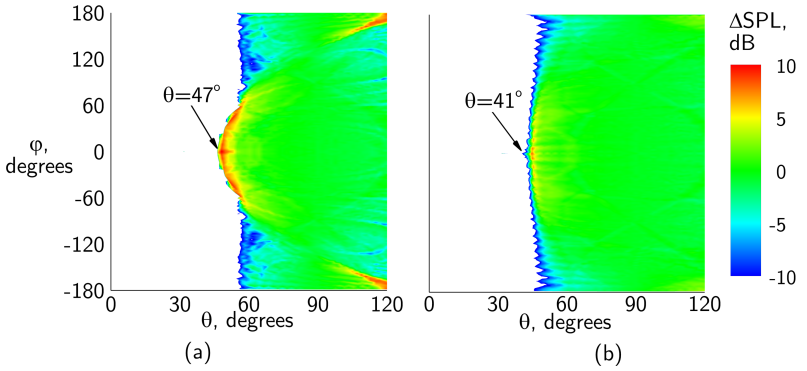

Figure 4.4 – ΔSPL contours for source positions (a) B and (b) D (see Figure 2.1 for the definition of φ and θ). Dependence of the zone of silence with source position for cold single-stream jet (*Case 2*). Arrows indicate the critical angle.

4.2.3 TET time scale

As shown in Chapter 2, an important difference between *Morris and Farassat (2002)* and *LRT (2011)* methods is the definition of the characteristic source frequency. With the adoption of the new time scale presented by Azarpeyvand (2008), *LRT (2011)* allows predictions of noise spectra in better agreement with experimental data. For instance, Figure 4.5 shows the numerical SPL for *Case 2* predicted by a modified *Morris and Farassat (2002)* in which the TET time scale (see Eq. (2.55)) was incorporated. This result indicates that information about the turbulence statistics incorporated in the TET time scale result in more accurate noise predictions.

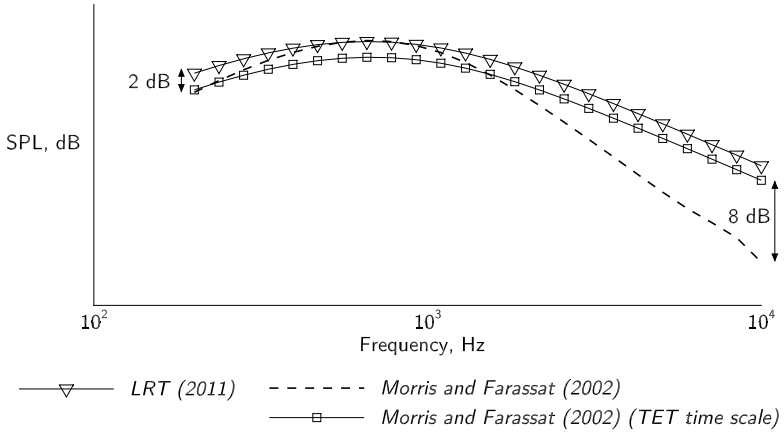

Figure 4.5 – SPL for *Case 2*. Comparison between the methods *LRT (2011)* and the modified *Morris and Farassat (2002)* using the TET time scale. See Figure 4.3, where the results for *LRT (2011)* are not distinguishable from experimental data.

4.3 HEATED JETS

As discussed in Chapter 1, the reduction of jet noise achieved by the increase of the bypass ratio (BPR) in turbofans can be understood with the study of cold jets. However, as the efficiency of increasing BPR is reaching a limit and considering that jets created by aircraft engines are heated, it is necessary to study noise emitted by heated jets. In this section, *Cases 4* and *5* are employed to analyse how the source models perform for single-stream heated jets and how gradients in the speed of sound affect refraction in these jets.

4.3.1 Temperature ratio

The temperature ratio (TR) is defined as the ratio between the fluid temperature at the nozzle exit and the temperature of the ambient air. The TR effect depends on the Mach number, as shown in Figure 4.6. In addition, Figures 4.7 and 4.8 show that current methods can predict with good accuracy the noise spectra. However, as the source strength models ignore the entropic term, the constants must be calibrated as a function of TR and Mach number. Therefore, the study of the entropic term in heated jets is an important requirement for the source strength modelling.

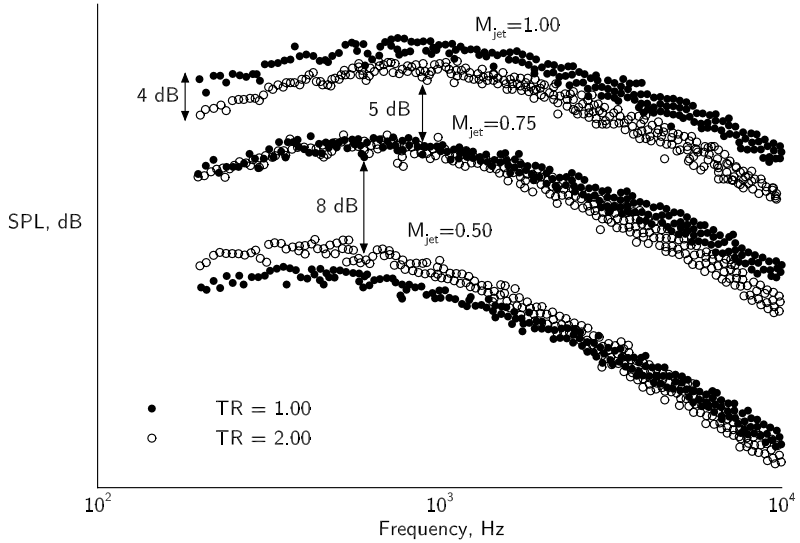

Figure 4.6 – Experimental SPL for cold and heated single-stream jets. Dependence of the temperature ratio effect with Mach number. Experimental data from (ILáRIO, 2011).

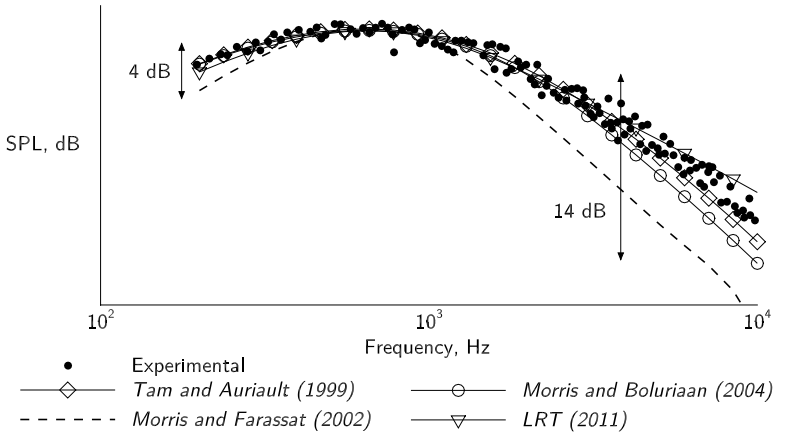

Figure 4.8 – SPL for heated single-stream jet with $M_{jet} = 0.75$, TR = 2.00 (*Case 5*). Experimental data from (ILáRIO, 2011).

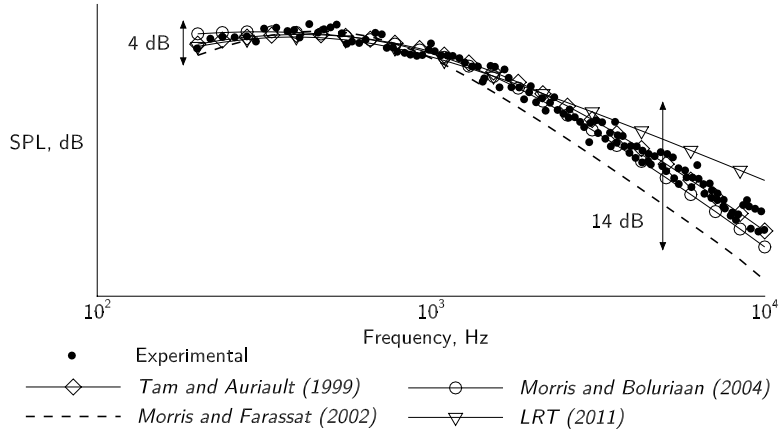

Figure 4.7 – SPL for heated single-stream jet with $M_{jet} = 0.50$, TR = 2.00 (*Case 4*). Experimental data from (ILáRIO, 2011).

4.3.2 Sound speed gradient

Many theories developed to study jet noise assume a constant sound speed throughout the jet (LIGHTHILL, 1952; GOLDSTEIN, 1976), which is valid for isothermal jets. However, it is known that the sound speed gradient must be considered when analysing the refraction effects in heated jets. Figure 4.9 shows the ΔSPL for rays traced from source position A based on RANS results of two flow conditions: (a) complete RANS solution for the heated jet (*Case 5*); (b) modified RANS solution with a constant speed of sound throughout the jet. The assumption of a constant speed of sound results in a difference of 9° in the critical angle, confirming the importance of this aspect in heated jets. Complementing the analysis, Figure 4.10 shows the path of 200 rays launched from source position A for the two flow conditions; rays are launched in the $x_1 - x_2$ plane with $x_3 = 0$, rendering a visualization of the zone of silence.

Although these results are known in the literature, the use of a ray tracing method makes it possible to visualize the effect of the sound speed gradient in the refraction of sound.

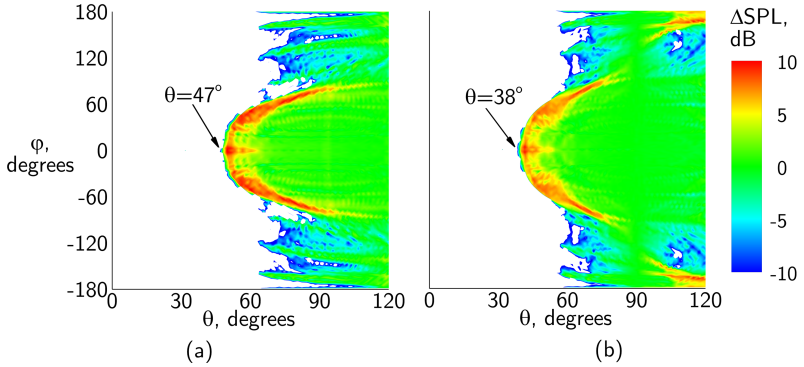

Figure 4.9 – ΔSPL contours for source positions A with (a) complete RANS solution (*Case 5*) and (b) modified RANS solution with a constant speed of sound. Arrows indicate the critical angle.

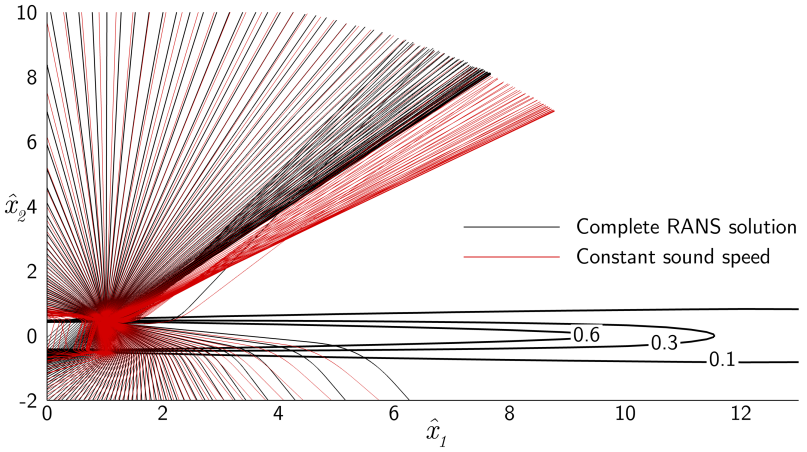

Figure 4.10 – Path for 200 rays emitted from source position A (*Case 5*). Emission angles are equally spaced in the range: $0° < \theta < 360°$ and $\varphi = 0°$.

4.4 DUAL-STREAM JETS

In this section, predictions for jet noise reduction achieved by a turbofan engine are analyzed with reference to experimental data for cold dual-stream jets presented by Ilário (2011). Two dual-stream jets with similar thrust output are chosen for comparison: a dual-stream

jet with a velocity ratio (VR) of unity, emulating a turbojet engine; and a dual-stream jet with VR = 0.60, representing a turbofan engine.

For a single-stream jet, the thrust output is proportional to $M_{jet}^2 D_{jet}^2$. For dual-stream jets the same relation is adopted, but considering the jet Mach number, M_{jet}, as the area-weighted Mach number between primary and secondary streams,

$$M_{jet} = \frac{M_{jet,p} D_{jet,p}^2 + M_{jet,s} \left(D_{jet,s}^2 - D_{jet,p}^2 \right)}{D_{jet,s}^2}, \tag{4.1}$$

where the subscript p relates to the primary stream and s to the secondary stream. The secondary-stream diameter, $D_{jet,s}$, is considered for the thrust output evaluation.

Table 4.5 summarizes values for the variables of Equation (4.1) and the thrust coefficient, which is defined as $M_{jet}^2 D_{jet}^2$. Figure 4.11 shows the experimental SPL for cases in Table 4.5. A decrease of 16dB in the maximum SPL, which represents a six-fold decrease in the acoustic pressure amplitude, is achieved at the expense of a thrust output reduction of 20%.

Table 4.5 – Information about dual-stream jets and the corresponding thrust coefficient.

VR	$M_{jet,p}$	$M_{jet,s}$	$D_{jet,p}$	$D_{jet,s}$	M_{jet}	Thrust coefficent
1.00	0.84	0.84	0.033m	0.058m	0.84	$2.53 \times 10^{-3} m^2$
0.60	0.84	0.50	0.033m	0.075m	0.57	$2.05 \times 10^{-3} m^2$

4.4.1 Velocity ratio

Considering a single dual-stream nozzle geometry (Figure 4.1), Figures 4.12 and 4.13 show that the source models can predict the noise spectra reasonably well for two different velocity ratios. However, the empirical constants had to be calibrated for each case. As for the effect of temperature ratio presented in Section 4.3.1, the need for a new calibration indicates that the models are not capable of capturing the full complexity of jet noise generation in these dual-stream jets.

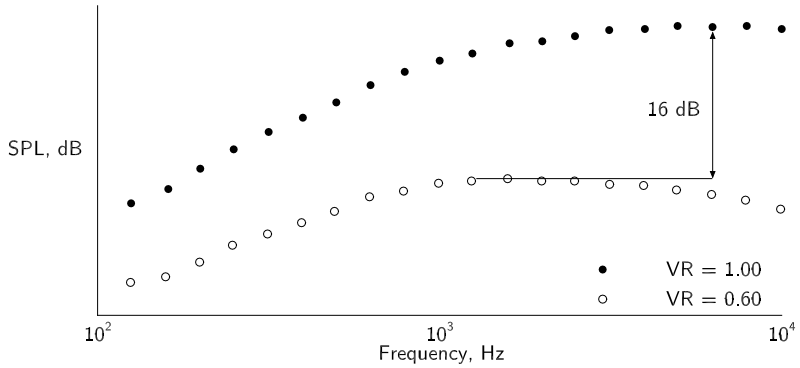

Figure 4.11 – Experimental SPL (ILáRIO, 2011) for two cold dual-stream jets with similar thrust output.

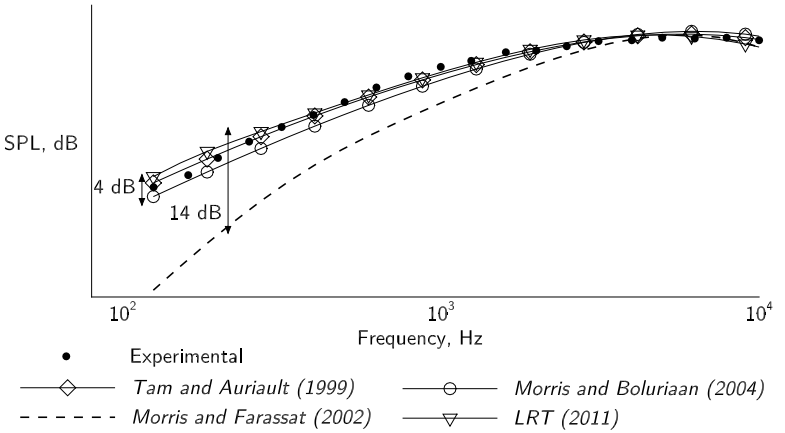

Figure 4.13 – SPL for cold dual-stream jet with VR = 1.00 (*Case 7*). Experimental data from (ILáRIO, 2011).

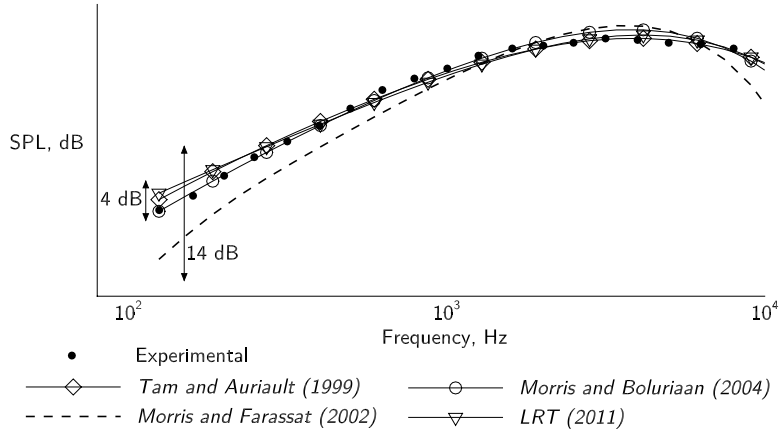

Figure 4.12 – SPL for cold dual-stream jet with VR = 0.60 (*Case 6*). Experimental data from (ILáRIO, 2011).

4.5 CHEVRON NOZZLES

The addition of chevrons to the jet nozzle is already being applied in commercial aircraft by major manufacturing companies. The effectiveness of chevrons in reducing jet noise relies on the fact that sound attenuation in the atmosphere increases with frequency. As the chevrons tend to shift the peak frequency towards higher frequencies, the total sound power reaching a distant observer is reduced. The effects of chevrons in the noise generation mechanisms are not easily predicted by scaling laws or empirical databases. In this area, flow prediction methods, such as RANS simulations, are valuable to further understand phenomena brought about by chevron nozzles.

4.5.1 Peak-frequency

Figure 4.14 shows measurements presented by Bridges and Brown (2004), confirming that chevron nozzles SMC001 and SMC006 increase the peak frequency when compared to the baseline SMC000 nozzle with no chevron. The chevrons in SMC006 have more penetration into the jet stream than in the SMC001 nozzle, which results in a further shift of the peak frequency to higher frequency. Figures 4.15 and 4.16 show that the source models predict the noise spectra for the chevron nozzles accurately. However, as for the heated single-stream and cold dual-stream jets, the empirical constants had to be calibrated for each case separately.

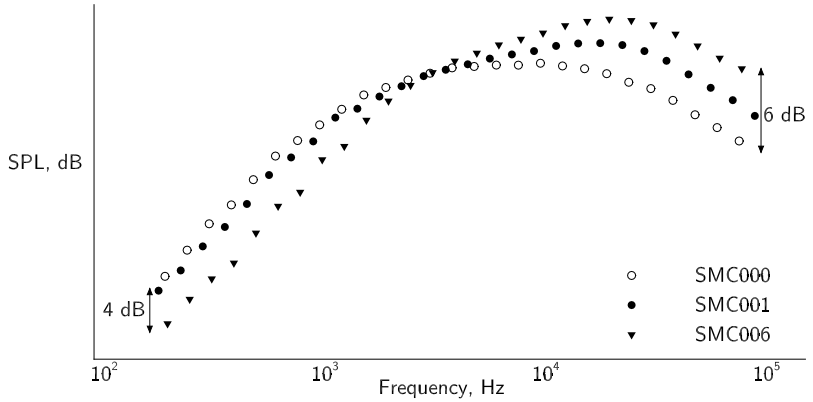

Figure 4.14 – Experimental SPL (BRIDGES; BROWN, 2004) for baseline nozzle (SMC000) and chevron nozzles with small penetration (SMC001) and large penetration (SMC006).

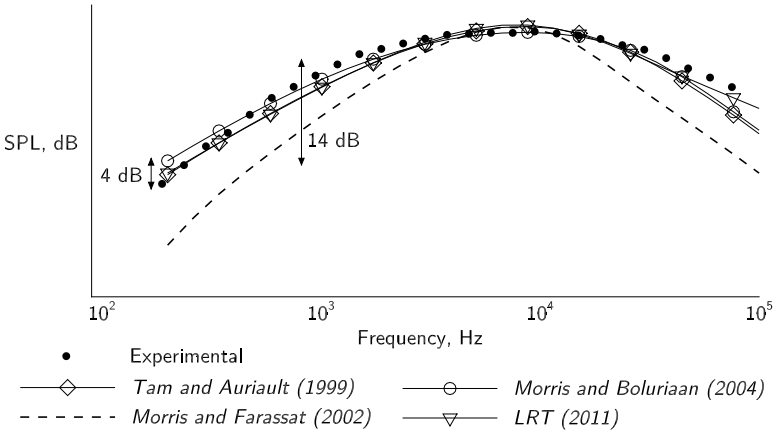

Figure 4.15 – SPL for SMC000 nozzle (*Case 8*). Experimental data from (BRIDGES; BROWN, 2004).

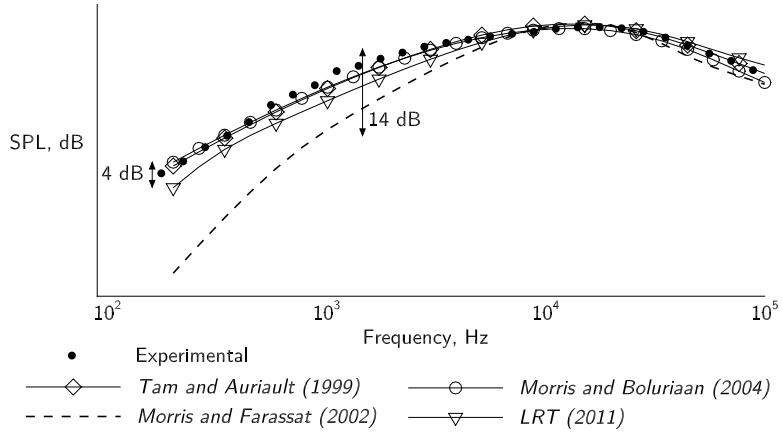

Figure 4.16 – SPL for SMC001 nozzle (*Case 9*); chevrons with small penetration. Experimental data from (BRIDGES; BROWN, 2004).

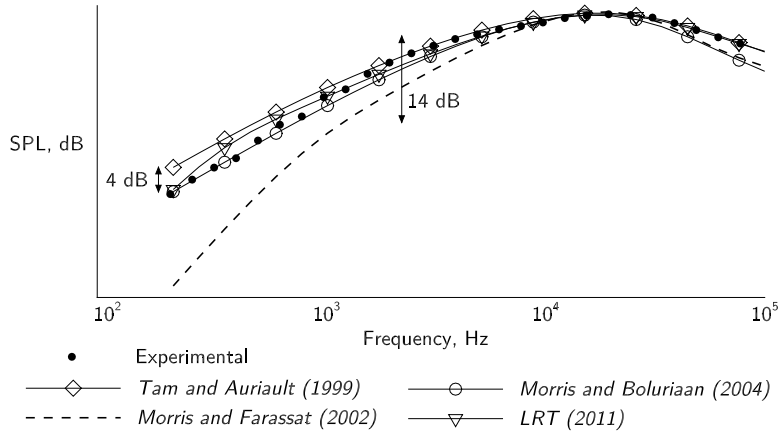

Figure 4.17 – SPL for SMC006 (*Case 10*); chevrons with large penetration. Experimental data from (BRIDGES; BROWN, 2004).

4.5.2 Asymmetry

The ray tracing method presented in Chapter 3 can be used to show asymmetric refraction patterns originated by chevrons. Although no significant source of noise is present in actual jets near the position G (see Figure 4.2), such a position is used because the shear layer is highly asymmetric in the x_2–x_3 plane at this axial position.

Figure 4.18 shows ΔSPL contours for source position G. As can be noted, the region defined by $60^\circ < \theta < 80^\circ$ is remarkably asymmetric and periodic due to the presence of six chevrons, with some regions of amplification and others unreachable to refracted rays. As expected, near $\theta = 90^\circ$ the refraction effects are less significant and for higher angles another asymmetric region is present.

Figure 4.19 shows paths for rays emitted from source position G. Rays are launched with emission angles of $\theta = 45^\circ$ and $0^\circ < \varphi < 360^\circ$, forming a cone around the jet axis before they are refracted in the jet shear layer. Figure 4.19 (a) shows the asymmetric path followed by the refracted rays that result in the far field asymmetries shown in Figure 4.18, whereas Figure 4.19 (b) illustrates the bending of the rays away from the jet axis, generating the zone of silence.

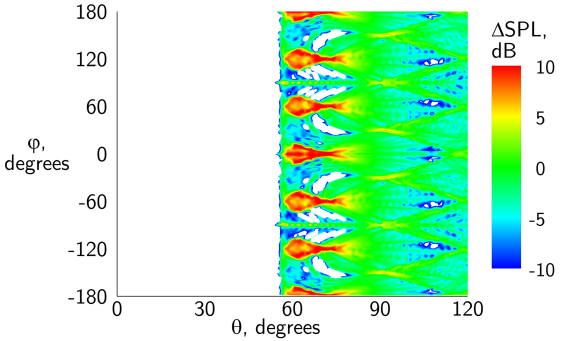

Figure 4.18 – Contours of ΔSPL for source position G (*Case 10*). Asymmetric patterns for rays emitted from source position G for the cold jet, chevron nozzle.

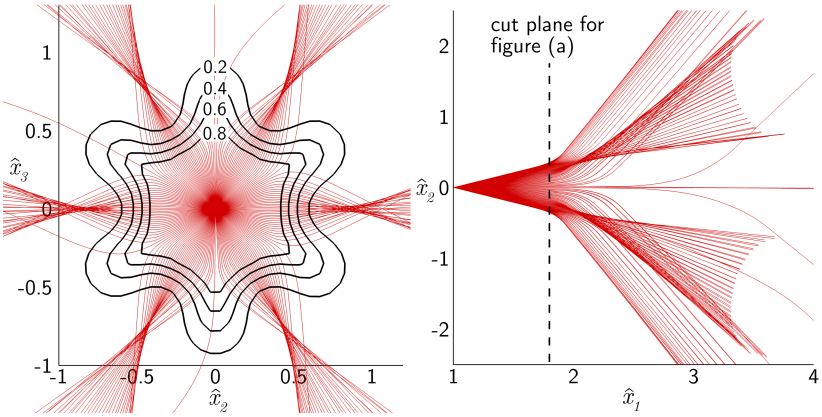

(a) (b)

Figure 4.19 – Three-dimensional paths for 200 rays emitted from source position G, with emission angles of $\theta = 45°$ and $0° < \varphi < 360°$. In (a), thick lines show constant values of $\langle U_1 \rangle / c_\infty$ on the plane indicated in (b). (a) x_1 view (b) x_3 view.

A similar analysis is carried out for the source positions B and B' to show the differences in the refraction between a source on the tip and the notch planes of the chevrons. Source position B' has the same axial and radial position as B, but it is rotated 90° around the x_1 axis.

Figure 4.20 shows the ΔSPL contours for source positions B and B'. By comparing Figures 4.20 (a) and (b), a shift of 90° can be noticed in the azimuthal angle (φ) of the general ΔSPL trend, as shown by the arrows indicating the critical angle at different azimuthal positions. This shift occurs because the sources are also shifted by 90°. However, the important result is the change in the shape of the ΔSPL contours near the critical angle. Whereas for source B there is a single and larger region of amplification near $\varphi = 0$, for position B' there is a smaller amplification region near $\varphi = 90°$ but two additional amplification regions near $\varphi = 30°$ and $\varphi = 150°$.

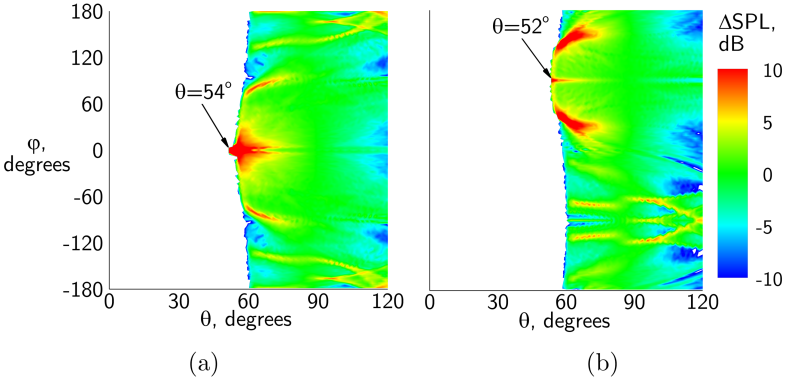

Figure 4.20 – Contours of ΔSPL for source positions (a) B and (b) B' (*Case 10*).

5 CONCLUSIONS

In this dissertation, RANS-based methods are assessed for their applicability in the prediction of noise emitted from subsonic jets. Such methods are associated with two steps: (i) the evaluation of the strength of sound sources and (ii) the evaluation of the effects of sound refraction. In this respect, four source strength models available in the literature are analyzed, and the ray tracing technique implemented by Ilário (2011) is adopted to study refraction effects.

5.1 SOURCE STRENGTH MODELS

The source strength models are derived from the Lighthill equation, represented by *Morris and Farassat (2002)* and *LRT (2011)*, and from the Linearized Euler Equations, as in *Tam and Auriault (1999)* and *Morris and Boluriaan (2004)*. Although *Morris and Farassat (2002)* and *LRT (2011)* have similar formulations, *LRT (2011)* predicts noise spectra in a significantly better agreement with experimental data. Conversely, the model formulations of *Tam and Auriault (1999)*, *Morris and Boluriaan (2004)* and *LRT (2011)* are quite different but result in small discrepancies in the predicted noise spectra.

The more accurate predictions of *LRT (2011)* in comparison with *Morris and Farassat (2002)* is caused by the use of the turbulent energy transfer (TET) time scale proposed by Azarpeyvand (2008). The results suggest that there is still room for improvement of source models through a better description of the relation between turbulence and aerodynamic noise.

Despite good agreement with experimental data, the source models rely on empirical constants that had to be calibrated for the majority of the investigated cases. This is an indication that some mechanisms of sound generation are not considered by such models.

It has been shown that all source models provide relations for SPL that scale with $k^{7/2}$. Additionally, by using the *LRT (2011)* formulation, an equation is derived to calculate the peak frequency of the noise spectrum. These relations could make it easier the calibration of the empirical constants and the optimization of new nozzle geometries.

The *LRT (2011)* method has a more straightforward derivation and requires fewer empirical constants than the other methods that showed the same level of accuracy (*Tam and Auriault (1999)* and *Morris and Boluriaan (2004)*). Therefore, *LRT (2011)* is considered the best source model for a numerical framework to predict jet noise.

The source models were simplified to consider only an observer at 90° to the jet axis and, therefore, not including any directional component of the sources. Nevertheless, the conclusions of the present study are valid for

other observer angles because most of the directional effects are caused by the sound-flow interaction and not by an inherent directional source strength.

The assessment of the four source models increased the confidence in the RANS-based methods considering the good agreement observed between predictions and experimental data of noise spectra. Moreover, it has been emphasized the importance of studies on fundamental aspects of turbulence, such as the ones that led to the definition of the TET time scale (AZARPEYVAND, 2008).

5.2 RAY TRACING METHOD

A three-dimensional ray tracing method was used to analyse the refraction of sound emitted from monopole sources in different positions within the jet. With the visualization of ray paths and contour plots of ΔSPL, three aspects of the refraction of sound in jets were analyzed: the dependence of the critical angle with the position of sources of sound, the importance of sound speed gradient in heated jets, and the asymmetry created by chevrons.

In contrast to use the Linearized Euler Equations or the Lilley Equation, which have analytical solution for simplified cases or rely on complex numerical solutions, the ray tracing method is based on a simple system of ordinary differential equations. The ray tracing method was already validated by Ilário (2011) and the present study corroborates its relevance as a computational aeroacoustics tool, mainly due to its simplicity and efficacy.

5.3 SUGGESTIONS FOR FUTURE WORK

Although the source models capture the effect of Mach number on noise emitted by cold single-stream jets, the empirical constants had to be calibrated for the case with $M_{jet} = 0.75$. Hence, the investigation of a universal set of empirical constants for cold single-stream jets using a broader database of experimental results is a relevant activity for future work.

For the remaining cases (heated single-stream, cold dual-stream, and cold chevron nozzles), the empirical constants had to be calibrated for each case. Ilário (2011) mapped the empirical constants as a function of Mach number and temperature ratio in an attempt to circumvent this problem. Such a mapping could be extended to include additional nozzle geometries and operating conditions, considering other parameters such as Reynolds number, thrust output, peak frequency, etc. For such a task, the development of an automatic calibration procedure should be devised.

Furthermore, DNS and LES could be used to study two important aspects: (i) the significance of the entropic term in the Lighthill stress tensor, discarded by *Morris and Farassat (2002)* and *LRT (2011)*, for heated jets; and (ii) the effect of turbulence anisotropy in turbulent jets issued from

chevron nozzles. These studies could improve the source models, reducing their dependence on empirical constants.

Although the proposed scaling of SPL with $k^{7/2}$ and the equation for the peak frequency were verified for the cold single-stream jets, these relations should also be assessed for other nozzle geometries and operating conditions.

Ilário (2011) validated the ray tracing method for sound propagation through a medium without solid boundaries. A natural extension of the method would consider acoustic pressure waves reflection in the presence of solid boundaries, which is important to evaluate the effects of wing, flaps and pylon on engine installation.

Finally, the ray tracing algorithm should be optimized. Since the solution for a single monopole source can take a few dozens of seconds, many hours are required to map the ΔSPL for the entire jet, which typically involves $\sim 10^3$ sources. As the computation of each ray path is carried out independently, the implementation of a parallel algorithm is straightforward and would decrease the computational processing time.

REFERENCES

ASTLEY, R. J.; GABARD, G. Computational Aero-Acoustics (CAA) for Aircraft Noise Prediction—Part A. *Journal of Sound and Vibration*, v. 330, n. 16, p. 3785–3786, 2011.

ASTLEY, R. J.; GABARD, G. Computational Aero-Acoustics (CAA) for Aircraft Noise Prediction—Part B. *Journal of Sound and Vibration*, v. 330, n. 17, p. 4081–4082, 2011.

AZARPEYVAND, M. *Some aspects of RANS based jet noise prediction*. Thesis (PhD) — University of Southampton, 2008.

BECKER, H. A.; MASSARO, T. A. Vortex evolution in a round jet. *Journal of Fluid Mechanics*, v. 31, n. 3, p. 435–448, 1968.

BODONY, D. J.; LELE, S. K. Current Status of Jet Noise Predictions Using Large-Eddy Simulation. *AIAA Journal*, v. 46, n. 2, 2008.

BRIDGES, J.; BROWN, C. A. Parametric testing of chevrons on single flow hot jets. In: *10th AIAA/CEAS Aeroacoustics Conference*. 2004.

CALLENDER, B.; GUTMARK, R.; MARTENS, S. A far–field investigation into chevron nozzle mechanisms and trends. In: *41st AIAA Aerospace Sciences Meeting and Exhibit*. 2003.

COLONIUS, T.; LELE, S. Computational aeroacoustics: progress on nonlinear problems of sound generation. *Progress in Aerospace Sciences*, v. 40, n. 6, p. 345–416, 2004.

ENGEL, R. C. *Análise de modelos de previsão do escoamento e do ruído acústico de jatos subsônicos gerados por bocais serrilhados*. Master's Thesis (Master) — UFSC, Florianópolis, 2012.

ERIKSSON, C. et al. Aircraft noise and incidence of hypertension. *Epidemiology*, v. 18, n. 6, p. 716–721, 2007.

FRANSSE, E. A. M. et al. Aircraft noise around a large international airport and its impact on general health and medication use. *Occupational and Environmental Medicine journal*, v. 61, p. 405–413, 2004.

FREUND, J. B.; FLEISCHMAN, T. G. Ray traces through unsteady jet turbulence. *International Journal of Aeroacoustics*, v. 1, n. 1, p. 83–96, 2002.

GOLDSTEIN, M. E. *Aeroacoustics*. : McGraw-Hill, 1976.

GREISER, E.; GREISER, C.; JANHSEN, K. Night-time aircraft noise increases prevalence of prescriptions of antihypertensive and cardiovascular drugs irrespective of social class—the cologne-bonn airport study. *Journal of Public Health*, v. 15, n. 5, p. 327–337, 2007.

HAINES, M. M. et al. Chronic aircraft noise exposure, stress responses, mental health and cognitive performance in school children. *Psychological Medicine*, v. 31, n. 2, p. 265–277, 2001.

HINZE, J. O. *Turbulence.* : McGraw-Hill, 1975.

HUNTER, C. A. *An Approximate Jet Noise Prediction Method based on Reynolds-Averaged Navier-Stokes Computational Fluid Dynamics Simulation.* Thesis (PhD) — The George Washington University, 2002.

ICAO. *Environemental Report: Aviation and Climate Change.* Québec, Canada, 2010. <http://www.icao.int/icao/en/env2010/environmentreport_2010.pdf>.

ILáRIO, C. R. S. *Development of a novel RANS-based method for the computational aeroacoustics of high speed jets.* Thesis (PhD) — Universidade de São Paulo, São Paulo, 2011.

JARUP, L. et al. Hypertension and exposure to noise near airports: the hyena study. *Environmental Health Perspectives*, v. 116, n. 3, 2008.

KARABASOV, S. A. Understanding jet noise. *Philosophical Transactions of the Royal Society of London*, v. 368, n. 3593-3608, 2010.

KARABASOV, S. A. et al. Jet Noise: Acoustic Analogy informed by Large Eddy Simulation. *AIAA Journal*, v. 48, n. 7, p. 1312–1325, 2010.

KHAVARAN, A.; BRIDGES, J. Modeling of turbulence generated noise in jets. In: *10th AIAA/CEAS Aeroacoustics Conference.* 2004.

KHAVARAN, A.; KREJSA, E. A. On the role of anisotropy in turbulent mixing noise. In: *4th AIAA/CEAS Aeroacoustics Conference.* 1998.

KHAVARAN, A.; KREJSA, E. A.; KIM, C. M. *Computation of Supersonic Jet Mixing Noise for an Axisymmetric CD Nozzle Using k-epsilon Turbulence Model.* Cleveland, EUA, 1992.

LIGHTHILL, M. J. On sound generated aerodynamically. I. General theory. *Proceedings of the Royal Society of London. Series A. Mathematical and Physical Sciences*, v. 211, n. 1107, 1952.

LIGHTHILL, M. J. On sound generated Aerodynamically. II. Turbulence as a Source of Sound. *Proceedings of the Royal Society of London. Series A. Mathematical and Physical Sciences*, v. 222, n. 1148, 1954.

LILLEY, G. M. On the noise from jets. In: *AGARD Conference Proceedings No 131 on Noise Mechanisms.* 1974.

LUSH, P. A. Measurements of subsonic jet noise and comparison with theory. *Journal of Fluid Mechanics*, v. 46, n. 3, 1971.

MATHIEU, J.; SCOTT, J. *An Introduction to Turbulent Flow.* : Cambridge University Press, 2000.

MEAD, C. J.; COPPLESTONE, R. A. *Further investigation of concepts for reducing the exhaust noise of HBPR aero-engines.* 1998.

MORREL, S.; TAYLOR, R.; LYLE, D. A review of health effects of aircraft noise. *Australian and New Zealand Journal of Public Health*, v. 21, n. 2, 1997.

MORRIS, P. J.; BOLURIAAN, S. The Prediction of Jet Noise From CFD Data. In: *10th AIAA/CEAS Aeroacoustics Conference*. 2004.

MORRIS, P. J.; FARASSAT, F. Acoustic Analogy and Alternative Theories for Jet Noise Prediction. *AIAA Journal*, v. 40, n. 4, 2002.

NASA. *Making future commercial aircraft quieter*. URL: http://www.nasa.gov/centers/glenn/about/fs03grc.html [Accessed 8 May 2013], 1999.

PATWARI, N.; DURGIN, G.; RAPPAPORT, T. S. An advanced 3d ray launching method for wireless propagation prediction. In: *IEEE 47th Vehicular Technology Conference*. 1997.

PIERCE, A. D. *Acoustics: An Introduction to Its Physical Principles and Applications*. : McGraw-Hill, 1981.

POPE, S. B. *Turbulent flows*. : Cambridge University Press, 2000.

PRESS, W. H. et al. *Numerical Recipes in Fortran 77*. : Cambridge University Press, 1997.

SHIN, K.; HAMMOND, J. K. *Fundamentals of Signal Processing For Sound and Vibration Engineers*. Chichester: John Wiley & Sons, 2008.

SMITH, M. J. T. *Aircraft Noise*. : Cambridge University Press, 1989.

SPALART, P. R.; SHUR, M. L.; STRELETS, M. K. Identification of sound sources in large-eddy simulations of jets. In: *13th AIAA/CEAS Aeroacoustics Conference*. 2007.

TAM, C. K. W. Computational Aeroacoustics: Issues and Methods. *AIAA Journal*, v. 33, n. 10, 1995.

TAM, C. K. W. Recent advances in computational aeroacoustics. *Fluid Dynamics Research*, v. 38, 2006.

TAM, C. K. W.; AURIAULT, L. Jet mixing noise from fine-scale turbulence. *AIAA Journal*, v. 37, n. 2, 1999.

TAM, C. K. W. et al. The sources of jet noise: experimental evidence. *Journal of Fluid Mechanics*, v. 615, p. 253–292, 2008.

TRITTON, D. J. *Physical Fluid Dynamics*. : Oxford University Press, 1988.

WANG, M.; FREUND, J. B.; LELE, S. K. Computational Prediction of Flow-Generated Sound. *Annual Review of Fluid Mechanics*, v. 38, n. 1, p. 483–512, jan. 2006.

WEI, M.; FREUND, J. B. A noise-controlled free shear flow. *Journal of Fluid Mechanics*, v. 546, p. 123–152, 2006.

XIA, H.; TUCKER, P. G.; EASTWOOD, S. Large-eddy simulations of chevron jet flows with noise predictions. *International Journal of Heat and Fluid Flow*, 2009.

APPENDIX A – Numerical solution of the Reynolds-averaged Navier–Stokes equations

The solution of the RANS equations used in this dissertation were developed by Ilário (2011) and Engel (2012). In Table A.1, information about the numerical simulations is presented. The reader is referred to the original references for further information.

Table A.1 – Information about the RANS equations solutions.

Case	Domain type	Number of volumes	Domain size[a]	Turbulence model	Commercial code employed	Reference
1	2D[b]	$\mathbf{8 \times 10^3}$	$\mathbf{(47 \times 210)}\ D_{jet}$	standard $\boldsymbol{k-\varepsilon}$	FLUENT 6.3.26	(ILáRIO, 2011)
2						
3						
4						
5						
6	2D[b]	$\mathbf{120 \times 10^3}$	$\mathbf{(47 \times 210)}\ D_{jet}$	$\boldsymbol{k-\varepsilon}$ cubic	CFD++	(ILáRIO, 2011)
7						
8	3D	$\mathbf{4000 \times 10^3}$	$\mathbf{(15 \times 50)}\ D_{jet}$	RSTM[c]	CFD++	(ENGEL, 2012)
9	3D	$\mathbf{4000 \times 10^3}$	$\mathbf{(15 \times 50)}\ D_{jet}$	$\boldsymbol{k-\varepsilon}$ cubic	CFD++	(ENGEL, 2012)
10						

[a] Presented as the dimensions of a cylinder aligned with the jet axis: base radius × length.
[b] Rotated to generate 3D results, necessary to the computational code shown in Appendix B.
[c] Reynolds-stress transport model.

APPENDIX B – Computational code

The source models presented in Chapter 2 were implemented in a FORTRAN 90 computational code. The main program, presented below in File B.1, is responsible for the evaluation of the SPL spectrum, after reading the numerical RANS solution and the empirical constants. The code was compiled with GNU Fortran (GCC) 4.7.2 in a Windows 7 environment with the following command line:

```
gfortran -o jetnpt.exe jetnpt.f90 -fopenmp
```

where `-fopenmp` is the compiler flag to enable parallel processing. In Table B.1 information about the CPU time is presented.

Table B.1 – CPU time information.

Case	Number of volumes	CPU time[a]	Elapsed real time[a]
1	1408000	∼80 s	∼8 s
10	3985200	∼210 s	∼22 s

[a] Using a 12-processors workstation.

File B.1 – `jetnpt.f90`

```
1  !Victor H. P. da Rosa
2  !written in standard FORTRAN 90
3  program jetnpt
4      implicit none
5      real(kind=8) :: time_start, time_finish
6      real(kind=8), parameter :: pi = dacos(-1.d0)
7      !input parameters
8      integer :: nx, ny, nz, header_lines, n_freq, n_nodes
9      real(kind=8) :: f_min, f_max, R, C_0, RHO_0, Dj, A,
           C_L_TAM, &
10         C_TAU_TAM, C_TAU_MORRIS, A2_CL3, C_L_LRT, C_TAU_LRT,
               B, &
11         C_L_MORRISBOLURIAAN, C_TAU_MORRISBOLURIAAN
12     logical :: run_tam, run_morris, run_lrt,
           run_morrisboluriaan
13     !cfd data
14     real(kind=8), dimension(:), allocatable :: U, RHO, TKE,
           EPS, C, DU, &
15         VOLUME
16     !frequency arrays
17     real(kind=8), dimension(:), allocatable :: f, SPLtam,
           SPLmorris, &
18         SPLlrt, SPLmorris_boluriaan, f_exp
19     !local variables
20     integer :: i_freq, i
21     character(100) :: file_name
```

```
22      real(kind=8) :: Uj, Mj, TR
23      !local functions
24      real(kind=8) :: tam, morris, lrt, morris_boluriaan
25      real(kind=8) :: max_SPL_f, dummy
26      !
27      call cpu_time(time_start)
28      do i=1,100
29          print *,
30      end do
31      print *, '--- JetNPT - Jet Noise Prediction Tool ---'
32      print *,
33      call read_parameters(nx, ny, nz, header_lines, n_freq,
            f_min, f_max, R, &
34          C_0, RHO_0, Dj, run_tam, A, C_L_TAM, C_TAU_TAM,
                run_morris, &
35          C_TAU_MORRIS, A2_CL3, run_lrt, C_L_LRT, C_TAU_LRT,
                run_morrisboluriaan,&
36          B, C_L_MORRISBOLURIAAN, C_TAU_MORRISBOLURIAAN,
                n_nodes)
37      !
38      if (run_tam) then
39          print *, 'Solving TamAuriault.'
40      end if
41      if (run_morris) then
42          print *, 'Solving MorrisFarassat.'
43      end if
44      if (run_lrt) then
45          print *, 'Solving LRT.'
46      end if
47      if (run_morrisboluriaan) then
48          print *, 'Solving MorrisBoluriaan.'
49      end if
50      !
51      allocate(f(n_freq),f_exp(n_freq))
52      !frequency array: n_freq elements equally spaced in
            linear space
53      do i_freq = 1, n_freq
54          f(i_freq) = (f_max-f_min) * real(i_freq-1) / real(
                n_freq - 1) + f_min
55      end do
56      !frequency array: n_freq elements equally spaced in log
            space
57      f_exp(1) = log10(f_min)
58      f_exp(n_freq) = log10(f_max)
59      do i_freq = 2, n_freq-1
60          f_exp(i_freq) = (f_exp(n_freq)-f_exp(1)) * &
61              real(i_freq-1) / real(n_freq - 1) + f_exp(1)
62      end do
63      f = 10.d0**f_exp
64      !
65      allocate(U(n_nodes), RHO(n_nodes), TKE(n_nodes), EPS(
            n_nodes), &
```

```
66          C(n_nodes),DU(n_nodes), VOLUME(n_nodes))
67      allocate(SPLtam(n_freq), SPLmorris(n_freq), SPLlrt(
            n_freq), &
68          SPLmorris_boluriaan(n_freq))
69      !
70      call read_cfd_input(nx, ny, nz, header_lines, n_nodes, U
            , RHO, TKE, &
71          EPS, C, DU, VOLUME)
72      !
73      Uj = maxval(U)
74      Mj = Uj/C_0
75      TR = (maxval(C)/C_0)**2.0d0
76      print *,
77      print *, 'Uj = ', Uj
78      print *, 'Mj = ', Mj
79      print *, 'TR =', TR
80      !
81      !parallel frequency loop
82      print *,
83      print *, 'Starting frequency loop.'
84  !$OMP PARALLEL DO SCHEDULE(STATIC)
85      do i_freq = 1, n_freq
86          if (run_tam) then
87              SPLtam(i_freq) = tam(f(i_freq), n_nodes, R,
                    RHO_0, C_0, &
88                  U, RHO, TKE, EPS, VOLUME, A, C_L_TAM,
                        C_TAU_TAM)
89          end if
90          if (run_morris) then
91              SPLmorris(i_freq) = morris(f(i_freq), n_nodes, R
                    , RHO_0, &
92                  C_0, RHO, TKE, EPS, VOLUME, C_TAU_MORRIS,
                        A2_CL3)
93          end if
94          if (run_lrt) then
95              SPLlrt(i_freq) = lrt(f(i_freq), n_nodes, R,
                    RHO_0, C_0, &
96              RHO, TKE, EPS, VOLUME, Dj, C_L_LRT, C_TAU_LRT)
97          end if
98          if (run_morrisboluriaan) then
99              SPLmorris_boluriaan(i_freq) = morris_boluriaan(f
                    (i_freq), &
100                 n_nodes, R, RHO_0, C_0, TKE, EPS, VOLUME, B,
                        &
101                 C_L_MORRISBOLURIAAN, C_TAU_MORRISBOLURIAAN)
102         end if
103         print *,  'f(', i_freq,') = ', f(i_freq)
104     end do
105 !$OMP END PARALLEL DO
106     !
107     ! Exporting results
108     if (run_tam) then
```

```
109         file_name = 'res_TamAuriault.dat'
110         call export_results(n_freq, f, SPLtam, len(file_name
                ), file_name)
111         print *, 'Solved TamAuriault.'
112     end if
113     if (run_morris) then
114         file_name = 'res_MorrisFarassat.dat'
115         call export_results(n_freq, f, SPLmorris, len(
                file_name), file_name)
116         print *, 'Solved MorrisFarassat.'
117     end if
118     if (run_lrt) then
119         file_name = 'res_LRT.dat'
120         call export_results(n_freq, f, SPLlrt, len(file_name
                ), file_name)
121         print *, 'Solved LRT.'
122     end if
123     if (run_morrisboluriaan) then
124         file_name = 'res_MorrisBoluriaan.dat'
125         call export_results(n_freq, f, SPLmorris_boluriaan,
                len(file_name), &
126         file_name)
127         print *, 'Solved MorrisBoluriaan.'
128     end if
129     !
130     dummy = max_SPL_f(n_nodes, TKE, EPS, VOLUME, Dj, C_L_LRT
            , C_TAU_LRT)
131     print *, '--- End of calculation ---'
132     !read *,
133     !
134     call cpu_time(time_finish)
135     print *, 'Elapsed time = ', time_finish-time_start, '
            seconds.'
136 end program jetnpt
137 !
138 subroutine read_parameters(nx, ny, nz, header_lines, n_freq,
        f_min, f_max, R, &
139     C_0, RHO_0, Dj, run_tam, A, C_L_TAM, C_TAU_TAM,
            run_morris, C_TAU_MORRIS, &
140     A2_CL3, run_lrt, C_L_LRT, C_TAU_LRT, run_morrisboluriaan
            , B, &
141     C_L_MORRISBOLURIAAN, C_TAU_MORRISBOLURIAAN, n_nodes)
142     implicit none
143     !input variables
144     !output variables
145     integer, intent(out) :: nx, ny, nz, header_lines, n_freq
            , n_nodes
146     real(kind=8), intent(out) :: f_min, f_max, R, C_0, RHO_0
            , Dj, A, &
147         C_L_TAM, C_TAU_TAM, C_TAU_MORRIS, A2_CL3, C_L_LRT,
                C_TAU_LRT, B, &
148         C_L_MORRISBOLURIAAN, C_TAU_MORRISBOLURIAAN
```

```
149     logical, intent(out) :: run_tam, run_morris, run_lrt,
            run_morrisboluriaan
150     !
151     open(unit=1, file='parameters.dat', form='formatted')
152     read(1,*) nx
153     read(1,*) ny
154     read(1,*) nz
155     read(1,*) header_lines
156     read(1,*) n_freq
157     read(1,*) f_min
158     read(1,*) f_max
159     read(1,*) R
160     read(1,*) C_0
161     read(1,*) RHO_0
162     read(1,*) Dj
163     read(1,*) run_tam
164     read(1,*) A
165     read(1,*) C_L_TAM
166     read(1,*) C_TAU_TAM
167     read(1,*) run_morris
168     read(1,*) C_TAU_MORRIS
169     read(1,*) A2_CL3
170     read(1,*) run_lrt
171     read(1,*) C_L_LRT
172     read(1,*) C_TAU_LRT
173     read(1,*) run_morrisboluriaan
174     read(1,*) B
175     read(1,*) C_L_MORRISBOLURIAAN
176     read(1,*) C_TAU_MORRISBOLURIAAN
177     close(1)
178     !
179     n_nodes = nx*ny*nz
180     !
181 end subroutine read_parameters
182 !
183 subroutine read_cfd_input(nx, ny, nz, header_lines, n_nodes,
        U, RHO, TKE, &
184     EPS, C, DU, VOLUME)
185     implicit none
186     !input variables
187     integer, intent(in) :: nx, ny, nz, header_lines, n_nodes
188     !output variables
189     real(kind=8), dimension(n_nodes) :: U, RHO, TKE, EPS, C,
            DU, VOLUME
190     !local variables
191     real(kind=8), dimension(n_nodes) :: X, Y, Z, dx, dy, dz
192     integer :: i_node, i, j, k
193     !
194     print *, 'Reading CFD_input_3D.bin'
195     open(unit = 20, status='old', file='CFD_input_3D.bin',
            form='unformatted', &
196         access='sequential')
```

```
197       read(20) X
198       read(20) Y
199       read(20) Z
200       read(20) U
201       read(20) RHO
202       read(20) TKE
203       read(20) EPS
204       close(20)
205       print *, 'Finished reading CFD_input_3D.bin'
206       dx(:) = X(2:nx)-X(1:nx-1)!the same as: dx(i) = X(i+1)-X(
              i), for i=1,nx-1
207       dy(:) = Y(2:ny)-Y(1:ny-1)
208       dz(:) = Z(2:nz)-Z(1:nz-1)
209       dx(nx) = 0.d0
210       dy(ny) = 0.d0
211       dz(nz) = 0.d0
212       !
213       i_node = 0
214       do k = 1, nz
215           do j = 1, ny
216               do i = 1,nx
217                   i_node = i_node + 1
218                   VOLUME(i_node) = dx(i)*dy(j)*dz(k)
219               end do
220           end do
221       end do
222       !avoid zero values for TKE and EPS
223       where(TKE.le..00001d0) TKE = .00001d0
224       where(EPS.le..00001d0) EPS = .00001d0
225   end subroutine read_cfd_input
226   !
227   function tam(f, n_nodes, R, RHO_0, C_0, U, RHO, TKE, EPS,
          VOLUME, A, C_L, C_TAU)
228       implicit none
229       !input
230       integer, intent(in) :: n_nodes
231       real(kind=8), intent(in), dimension(n_nodes) :: U, RHO,
              TKE, EPS, &
232           VOLUME
233       real(kind=8), intent(in):: f, R, RHO_0, C_0
234       !local
235       real(kind=8), parameter :: pi = dacos(-1.0d0)
236       real(kind=8), dimension(n_nodes) :: dS, fs, f_fs
237       real(kind=8) :: A, C_L, C_TAU, S, linear2dB, C
238       real(kind=8) :: tam
239       !
240       fs = EPS * (C_TAU * TKE)**(-1.d0)
241       f_fs = f/fs
242       !
243       C = (dsqrt(pi) / 9.d0) * (c_0**4.d0 * R**2.d0)**(-1.d0)
244       !
245       dS = C * A**2.d0 * C_L**3.d0 * C_TAU**(-3.d0) * RHO**2.
```

```
          d0 * &
246       TKE**(7.d0 / 2.d0) * f_fs**2.d0 * (1.d0 + 4.d0 * pi
              **2.d0 * &
247       f_fs**2.d0)**(-1.d0) * exp( -pi**2.d0 * C_L**2.d0 *
              &
248       C_TAU**(-2.d0) * TKE * U**(-2.d0) * f_fs**2.d0 ) &
249       * VOLUME
250     !
251     S = sum(dS) ! [W/m^2]
252     tam = linear2dB(S) ! [dB]
253     !
254 end function tam
255 !
256 function morris(f, n_nodes, R, RHO_0, C_0, RHO, TKE, EPS,
        VOLUME, &
257     C_TAU, A2_CL3)
258     implicit none
259     !input
260     integer, intent(in) :: n_nodes
261     real(kind=8), intent(in), dimension(n_nodes) :: RHO, TKE
            , EPS, VOLUME
262     real(kind=8), intent(in):: f, R, RHO_0, C_0
263     !local
264     real(kind=8), parameter :: pi = dacos(-1.0d0)
265     real(kind=8), dimension(n_nodes) :: dS, fs, f_fs
266     real(kind=8) :: A2_CL3, C_TAU, S, linear2dB, C
267     real(kind=8) :: morris
268     !
269     fs = EPS * (C_TAU * TKE)**(-1.d0)
270     !fs = 0.1016**(2.0d0/3.0d0)*EPS**(5.d0/3.d0) * TKE**(-2.
            d0) * C_TAU**(-1.d0)
271     f_fs = f/fs
272     !
273     C =  (pi**2.d0 / 9.d0) * (C_0**4.d0 * R**2.d0)**(-1.d0)
274     !
275     dS = C * A2_CL3 * C_TAU**(-3.d0) * RHO**2.d0 * TKE**(7.
            d0/2.d0) * &
276          (f_fs)**4.d0 * exp(-pi**2.d0 * f_fs**2.d0) &
277          * VOLUME
278     !
279     S = sum(dS) ! [W/m^2]
280     morris = linear2dB(S) ! [dB ref 1d-12 W/m2]
281 end function morris
282 !
283 function lrt(f, n_nodes, R, RHO_0, C_0, RHO, TKE, EPS,
        VOLUME, Dj, C_L, &
284     C_TAU)
285     implicit none
286     !input
287     integer, intent(in) :: n_nodes
288     real(kind=8), intent(in), dimension(n_nodes) :: RHO, TKE
            , EPS, &
```

```
289             VOLUME
290         real(kind=8), intent(in):: f, R, RHO_0, C_0, C_L, C_TAU
291         !local variables
292         real(kind=8), parameter :: pi = dacos(-1.d0)
293         real(kind=8) :: linear2DB
294         real(kind=8) :: S, Dj, C
295         real(kind=8), dimension(n_nodes) :: dS, fs, f_fs
296         real(kind=8) :: lrt
297         !
298         !fs - source frequency
299         fs = Dj**(2.d0/3.d0) * C_TAU**(-1.d0) * C_L**(-2.d0/3.d0
                ) &
300             * EPS**(5.d0/3.d0) * TKE**(-2.d0)
301         f_fs = f/fs
302         !
303         C = pi**(5.d0/2.d0) * 0.25d0 *  (C_0**4.d0 * R**2.d0)
                **(-1.d0)
304         !
305         dS = C * C_L**3.d0 * C_TAU**(-3.d0) * RHO**2.d0 * TKE
                **(7.d0/2.d0) &
306             * f_fs**4.d0 * dexp(-0.5d0*pi**2.d0 * f_fs**2.d0) &
307             * VOLUME
308         !
309         S = sum(dS)
310         lrt = linear2dB(S)
311     end function lrt
312     !
313     function morris_boluriaan(f, n_nodes, R, RHO_0, C_0, TKE,
            EPS, VOLUME, B, &
314         C_L, C_TAU)
315         implicit none
316         !input
317         integer, intent(in) :: n_nodes
318         real(kind=8), intent(in), dimension(n_nodes) :: TKE, EPS
                , VOLUME
319         real(kind=8), intent(in):: f, R, RHO_0, C_0, B, C_L,
                C_TAU
320         !local variables
321         real(kind=8), parameter :: pi = dacos(-1.d0)
322         real(kind=8) :: linear2DB
323         real(kind=8) :: S, C
324         real(kind=8), dimension(n_nodes) :: dS, fs, f_fs
325         real(kind=8) :: morris_boluriaan
326         !
327         fs = EPS * (C_TAU * TKE)**(-1.d0)
328         f_fs = f/fs
329         !
330         C = (4.d0 * pi**(3.d0/2.d0) / 27.d0) * RHO_0**2.d0 &
331             * (C_0**4.d0 * R**2.d0)**(-1.d0)
332         !
333         dS = C * B**2.d0 * (C_L/C_TAU) * TKE**(7.d0/2.d0) * f_fs
                **2.d0 &
```

```
334         * (1.d0 + 4.d0 * pi**2.d0 * f_fs**2.d0)**(-1.d0) &
335         * exp(-pi**2.d0 * (C_L/C_TAU)**2.d0 * TKE * C_0
                **(-2.d0) * f_fs**2.d0) &
336         * VOLUME
337     !
338     S = sum(dS)
339     morris_boluriaan = linear2dB(S)
340 end function morris_boluriaan
341 !
342 function max_SPL_f(n_nodes, TKE, EPS, VOLUME, Dj, C_L, C_TAU
        )
343     implicit none
344     !input
345     integer, intent(in) :: n_nodes
346     real(kind=8), intent(in), dimension(n_nodes) :: TKE, EPS
            , VOLUME
347     real(kind=8), intent(in):: C_L, C_TAU
348     !local variables
349     real(kind=8), parameter :: pi = dacos(-1.d0)
350     real(kind=8) :: linear2DB
351     real(kind=8) :: S, Dj, C
352     real(kind=8), dimension(n_nodes) :: dS, fs, f_fs
353     real(kind=8) :: peak_f, max_SPL, max_SPL_f
354     !
355     !fs - characteristic source frequency
356     fs = Dj**(2.d0/3.d0) * C_TAU**(-1.d0) * C_L**(-2.d0/3.d0
            ) &
357         * EPS**(5.d0/3.d0) * TKE**(-2.d0)
358     !
359     max_SPL = sum(TKE**(7.d0/2.d0)*VOLUME)
360     peak_f = sum((fs/pi) * TKE**(7.d0/2.d0) * VOLUME) &
361         / sum(TKE**(7.d0/2.d0) * VOLUME)
362     print *, 'maximum SPL', max_SPL
363     print *, 'peak f', peak_f
364 end function max_SPL_f
365 !
366 function linear2dB(S)
367     real(kind=8) :: linear2dB
368     real(kind=8), parameter :: P_ref = 2.0d-5
369     real(kind=8), intent(in) :: S
370     linear2dB = 10.d0 * dlog10(S/P_ref**2.d0)
371 end function linear2dB
372 !
373 subroutine export_results(n_freq, f, SPL, file_name_length,
        file_name)
374     implicit none
375     !input
376     integer, intent(in) :: n_freq, file_name_length
377     character(file_name_length), intent(in) :: file_name
378     real(kind=8), dimension(n_freq), intent(in) :: f, SPL
379     !local
380     integer :: i_freq
```

```
381     !
382     open(unit = 1, file = file_name)
383     do i_freq = 1, n_freq
384         write(1,*) f(i_freq), SPL(i_freq)
385     end do
386 end subroutine export_results
```